Article

Structure

Mg^{2+}-dependent mechanism of environmental versatility in a multidrug efflux pump

Graphical abstract

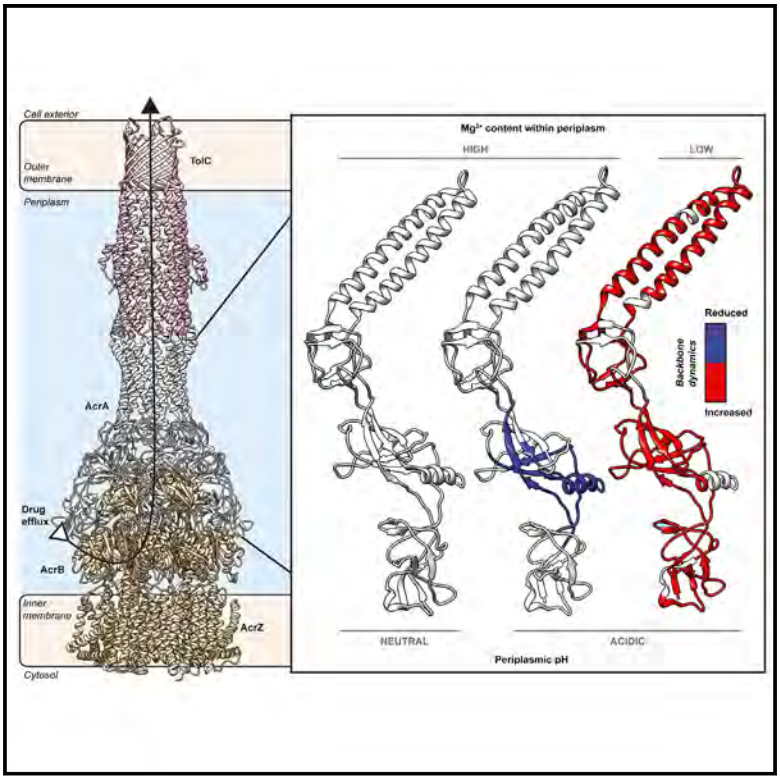

Highlights

- AcrA structural dynamics respond to shifting pH and Mg^{2+} periplasmic conditions
- Mg^{2+} is a stabilizing structural cofactor for the periplasmic adapter protein AcrA
- (De)protonation of a unique histidine modulates AcrA dynamics
- Histidine285 is vital for congruous AcrAB-TolC efflux pump activity between pH 5–8

Authors

Benjamin Russell Lewis, Muhammad R. Uddin, Katie M. Kuo, ..., James C. Gumbart, Helen I. Zgurskaya, Eamonn Reading

Correspondence

gumbart@physics.gatech.edu (J.C.G.), elenaz@ou.edu (H.I.Z.), e.reading@soton.ac.uk (E.R.)

In brief

RND multidrug efflux pumps have a critical role in innate and acquired antibiotic resistance in gram-negative bacteria. Russell Lewis et al. used a combination of hydrogen/deuterium exchange mass spectrometry, molecular dynamics simulations, and bacterial drug efflux assay investigations to uncover Mg^{2+} as an important mechanistic component in this pump class.

Russell Lewis et al., 2025, Structure *33*, 1–14
March 6, 2025
https://doi.org/10.1016/j.str.2024.12.012

CellPress

Please cite this article in press as: Russell Lewis et al., Mg^{2+}-dependent mechanism of environmental versatility in a multidrug efflux pump, Structure (2024), https://doi.org/10.1016/j.str.2024.12.012

Structure

CellPress
OPEN ACCESS

Article

Mg^{2+}-dependent mechanism of environmental versatility in a multidrug efflux pump

Benjamin Russell Lewis,[1,6] Muhammad R. Uddin,[2,6] Katie M. Kuo,[3,6] Laila M.N. Shah,[1] Nicola J. Harris,[1] Paula J. Booth,[1] Dietmar Hammerschmid,[1,4] James C. Gumbart,[3,5,*] Helen I. Zgurskaya,[2,*] and Eamonn Reading[1,4,7,*]

[1]Department of Chemistry, Britannia House, 7 Trinity Street, King's College London, London, SE1 1DB, UK
[2]Department of Chemistry and Biochemistry, University of Oklahoma, 101 Stephenson Parkway, Norman, OK 73019, USA
[3]School of Physics, Georgia Institute of Technology, 837 State Street NW, Atlanta, GA 30332, USA
[4]School of Biological Sciences, University of Southampton, Southampton, SO17 1BJ, UK
[5]School of Chemistry and Biochemistry, Georgia Institute of Technology, 901 Atlantic Drive NW, Atlanta, GA 30332, USA
[6]These authors contributed equally
[7]Lead contact
*Correspondence: gumbart@physics.gatech.edu (J.C.G.), elenaz@ou.edu (H.I.Z.), e.reading@soton.ac.uk (E.R.)
https://doi.org/10.1016/j.str.2024.12.012

SUMMARY

Tripartite resistance nodulation and cell division multidrug efflux pumps span the periplasm and are major drivers of multidrug resistance among gram-negative bacteria. Cations, such as Mg^{2+}, become concentrated within the periplasm and, in contrast to the cytoplasm, its pH is sensitive to conditions outside the cell. Here, we reveal an interplay between Mg^{2+} and pH in modulating the structural dynamics of the periplasmic adapter protein, AcrA, and its function within the prototypical AcrAB-TolC multidrug pump from *Escherichia coli*. In the absence of Mg^{2+}, AcrA becomes increasingly plastic within acidic conditions, but when Mg^{2+} is bound this is ameliorated, resulting instead in domain specific organization. We establish a unique histidine residue directs these dynamics and is essential for sustaining pump activity across acidic, neutral, and basic regimes. Overall, we propose Mg^{2+} conserves AcrA structural mobility to ensure optimal AcrAB-TolC function within rapidly changing environments commonly faced during bacterial infection and colonization.

INTRODUCTION

Antimicrobial resistance (AMR) is a major threat to global health, and is expected to reduce life expectancy globally by an average of 1.8 years over the next decade without proper action.[1] The resistance nodulation and cell division (RND) efflux pump protein superfamily significantly contributes to multidrug resistance in gram-negative bacteria, due to their ability to export an extensive range of chemically diverse molecules and reduce intracellular concentrations of antibiotics.[2–4] RND efflux pumps are tripartite assemblies that span the double membrane and periplasm of gram-negative bacteria, and AcrAB-TolC, from *E. coli*, is the classical RND efflux pump.[5–7] It consists of an inner membrane transporter AcrB—that is energized by the proton motive force—connected to an outer membrane factor (OMF) TolC by the periplasmic adapter protein (PAP) AcrA, also known as the membrane fusion protein (MFP), forming a 3:6:3 (AcrB:AcrA:TolC) complex stoichiometry (Figure 1A).[10,11] For efficient substrate efflux to occur, AcrA must have the structural mobility capable of transmitting conformational information between AcrB and TolC during substrate recognition and transport, while also possessing the stability needed for maintaining a continuous sealed channel.[12] With homologs across other gram-negative ESKAPE bacteria, enhanced mechanistic insight into this system can inform on wider RND behavior as well as emerging efforts to inhibit the protein class to restore antibiotic efficacy.[13–15]

The periplasmic environment AcrA resides in is distinct compared to the internal cytosolic and external environments of gram-negative bacteria; it has a pH closer to the outside of the cell, concentrated cation populations, such as Mg^{2+} (driven by the Donnan potential), and a peptidoglycan layer.[16] Critically, further understanding collective contributions of protons and Mg^{2+} becomes important when considering their putative fluctuations within the periplasm during the enteric journey of *E. coli* through a human gut (e.g., stomach pH 1.5–4.0 and intestines pH 4.0–7.5) and within the microenvironments of macrophage phagosomes.[8,17–20] Mg^{2+} not only has its role in the periplasm but is a crucial nutrient for *E. coli* function and survival, being identified as a physiological cofactor in various enzymatic reactions as well as having roles in membrane and ribosome stabilization, chemotaxis, cell mobility, cellular signaling, and pathogenesis.[21,22]

Previous investigations have shown that AcrA conformation is pH- and Mg^{2+}-sensitive[8,9,23] and that related heavy metal efflux RND (HME-RND) pump systems can interact with the divalent metal cations they export to induce conformational changes, i.e. Zn^{2+} by ZneCAB, and Cu^{+} and Ag^{+} by CusCBA.[24,25] However, it remains uncertain whether Mg^{2+} has a directive role within

Please cite this article in press as: Russell Lewis et al., Mg^{2+}-dependent mechanism of environmental versatility in a multidrug efflux pump, Structure (2024), https://doi.org/10.1016/j.str.2024.12.012

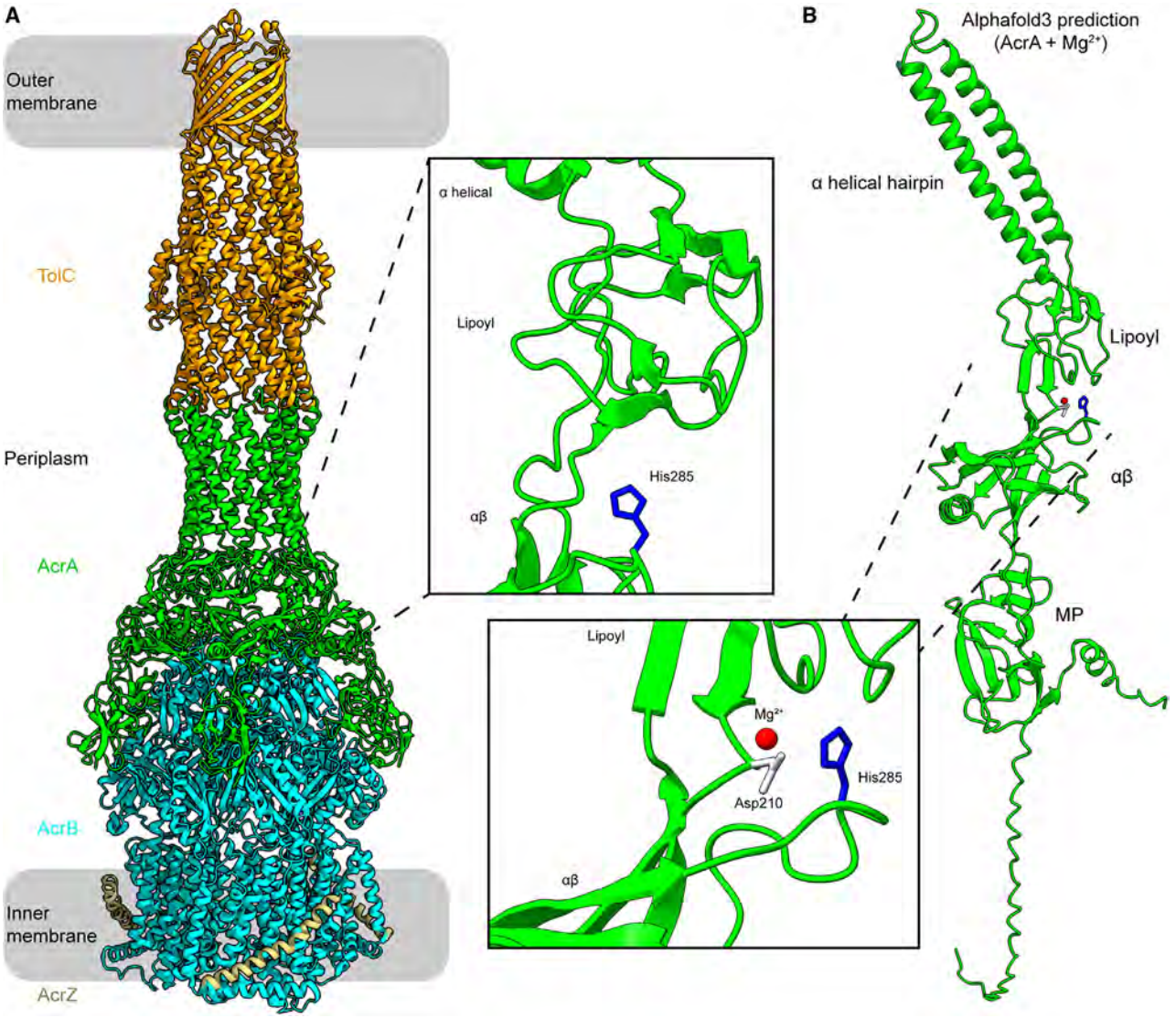

Figure 1. Predicted His285 and Mg^{2+} positioning within AcrA from the *Escherichia coli* AcrAB(Z)-TolC multidrug efflux pump

(A) Structure of AcrAB(Z)-TolC in the *E. coli* gram-negative cell envelope (PDB: 5O66). AcrB trimer is colored in cyan, AcrA trimer of dimers is colored in green, TolC trimer is colored in orange, and AcrZ is colored in gold. An insert shows the location of His285 (blue), previously suggested to be a conformational switch in AcrA.[8,9]

(B) AlphaFold3 prediction of the AcrA and Mg^{2+} complex. The best scoring model saw Mg^{2+} bind to Asp210, located between the lipoyl and αβ barrel domains and in close proximity to His285. The reported predicted template modeling (pTM) score and the interface predicted template modeling (ipTM) score were 0.59 and 0.73, respectively, and had a ranking score of 0.77. MP = membrane proximal domain.

RND multidrug efflux pump structure and function. Here, through a combination of hydrogen/deuterium exchange mass spectrometry (HDX-MS), molecular dynamics (MD) simulations, and biophysical investigations we uncover Mg^{2+} as a structural cofactor within the periplasmic adapter protein AcrA. We show that Mg^{2+} transforms the dynamics of AcrA when exposed to increased acidity but has little influence at neutral pH, and that without Mg^{2+}, acidification leads to backbone destabilization throughout the protein. In contrast, when Mg^{2+} is present then acidification causes domain-localized backbone stability. Mg^{2+}, therefore, directs the route pH-induced conformational alterations can take. This discovery harmonizes previous, seemingly conflicting, computational models, which found that protonation of a unique His285 residue within AcrA caused both extensive destabilization and localized stabilization of backbone hydrogen-bonding networks.[8] Using bacterial efflux assays, we go further to substantiate the importance of both Mg^{2+} and His285 for AcrA regulation, revealing that His285 is essential in ensuring AcrAB-TolC functions across a broad pH range (pH 5–8). Taken together, this work supports that AcrA recruits available protons and Mg^{2+} ions to ensure continued AcrAB-TolC function and bacterial survival, a process which may be general across related periplasmic protein adapter proteins also involved in multidrug efflux resistance.

Please cite this article in press as: Russell Lewis et al., Mg^{2+}-dependent mechanism of environmental versatility in a multidrug efflux pump, Structure (2024), https://doi.org/10.1016/j.str.2024.12.012

RESULTS

Motivated by the heightened concentration of protons and Mg^{2+} experienced within the *E. coli* periplasm, we explored the effect, and interplay, of Mg^{2+} and pH on AcrA structure-function. To simulate acidic and neutral periplasmic pH conditions during HDX-MS we investigated AcrA at pH 6.0 and 7.4, with and without the addition of 1 mM $MgCl_2$, with bacterial functional studies performed across a broader pH range of 5.0–8.0. Wild type, lipidated AcrA, was used for all functional assays and a previously established functional and soluble AcrA construct ($AcrA^S$), with its lipidation site removed by mutation, was used for structural and biophysical investigations as it provided the required sample homogeneity.[14,23] This delipidated AcrA construct was also utilized for MD simulations, with (de)protonation of the unique His285 residue used as a proxy for pH 7.4 and 6.0 conditions. His285 is located at the αβ barrel domain surface facing the lipoyl domain and is the only residue within AcrA that has a titratable protonation state change between mildly acidic and neutral regimes (Figure 1A). Using the Henderson–Hasselbalch equation and an estimated pKa of 5.89 for His285 (calculated using PROPKA),[26] then ∼44% of His285 will be protonated in solution at pH 6.0 compared to ∼3% at pH 7.4; HDX-MS is sensitive enough to assess backbone changes between these populations. More acidic regimes were not investigated by HDX-MS as it was previously shown that $AcrA^S$ exhibits undefined oligomerisation toward pH 5.0 *in vitro*,[9] which would complicate any HDX-MS interpretation, whereas $AcrA^S$ at pH 6.0 and 7.4 was previously characterized as a homogeneous monomer *in vitro*.[14]

Mg^{2+} is a possible AcrA cofactor

Mg^{2+} binding to proteins has been well considered.[27] As a hard metal, Mg^{2+} is prone to bind oxygens from the side chain carboxylate groups in Glu and Asp residues (these residues in AcrA are highlighted in Figure S1), with several classes of recognized Mg^{2+} cofactor sites that share an abundance of Glu and Asp residues found across diverse classes of enzymes.[27] To investigate whether AcrA could bind metal cations we first used *Me*Bi*Pred*—which uses machine learning algorithms to determine metal binding based on a protein primary sequence[28]—to explore binding to a variety of mono/di/trivalent metal cations, including Ca, Co, Cu, Fe, K, Mg, Mn, Na, Ni, and Zn. Only Mg^{2+} was identified as a binding metal (Table S1). Expansion of the *Me*Bi*Pred* analysis predicts Mg^{2+} binding to related, lipidated RND PAPs, indicating Mg^{2+} binding may be generic across this type. Indeed, when performing an analysis on the subcellular proteomes within the periplasmic space of *E. coli* K-12[29,30] (see STAR Methods), inner membrane lipoproteins (IMLPs) had the highest Mg^{2+} binding proportion predicted at 43.5%, compared to outer membrane lipoproteins (OMLPs, 21.6%), periplasmic proteins peripherally associated with IM (IM-peri, 29.2%) and soluble proteins located in the periplasm (periplasm, 23.6%) (Figure S2).

Building upon this further, AlphaFold3 was applied to AcrA and Mg^{2+} (Figure 1B). AlphaFold3 is capable of joint structure predictions of protein complexes with DNA/RNA, ligands, and ions.[31] It provides both a predicted template modeling (pTM) score and an interface predicted template modeling score (ipTM) as measures of accuracy for its ligand-protein structural interaction predictions. For AcrA and Mg^{2+}, the best scoring model (pTM = 0.59, ipTM = 0.73, and ranking score = 0.77) showed Mg^{2+} bound to Asp210, which is between the lipoyl and αβ barrel domains of AcrA and in close proximity to His285 (Figure 1B). Comparable scores were seen for ZneB and Zn^{2+}, a confirmed zinc binder, and other homologous PAPs were predicted to bind Mg^{2+} in similar areas as seen for AcrA (Figure S3).

Next, we expressed and purified AcrA in *E. coli* (see STAR Methods and Figures S4A and S4B) and used isothermal titration calorimetry (ITC) to verify AcrA binding to Mg^{2+} and found that qualitatively Mg^{2+} binds to AcrA similarly at both pH 6.0 and pH 7.4 (Figures S4C and S4D). Native MS analysis supports the occurrence of weak, and possibly multivalent, Mg^{2+} binding to $AcrA^S$ without modifying its oligomeric state (Figure S4E). When incubated with 100 μM $MgCl_2$ peak broadening was observed, characteristic of multiple Mg^{2+} ions remaining bound to the protein in the gas phase. Although, resolution of the quadrupole time-of-flight (Q-ToF) mass spectrometer used prevented exact stoichiometries being assigned. Circular dichroism (CD) spectroscopy was then used to evaluate secondary structure and thermal stability consequences of Mg^{2+} binding to AcrA.[32,33] Secondary structure content was indistinguishable in the presence or absence of $MgCl_2$ within the pH 7.4 condition, whereas at pH 6.0 inclusion of $MgCl_2$ caused an increase in β-sheet content (Figure S4F; Table S2). Interestingly, the related HME-RND periplasmic adapter protein, ZneB, had an increase in β-sheet content when bound to its Zn^{2+} cofactor.[24] We also performed CD thermal melts on $AcrA^S$ ± Mg^{2+}, which revealed Mg^{2+} binding did not significantly affect the thermal stability of $AcrA^S$ at either pH 6.0 or 7.4 (Figure S4G).

To better understand how AcrA is interacting with Mg^{2+}, we performed MD simulations on AcrA ± $MgCl_2$ or NaCl and monitored the occupancy of the ions across the different domains of $AcrA^S$ (Figure S5). Binding was observed for both Na^+ and Mg^{2+}, and although Mg^{2+} binding was found most localized to the same lipoyl domain site found by AlphaFold3, the simulations suggested that there are likely several other regions of AcrA that can interact with Mg^{2+}. Furthermore, cation binding site positions were not significantly affected by protonation of His285. Our previous MD simulations revealed free AcrA exhibited a range of orientations but had two main conformational basins[34]: one was a *cis*-like formation where the MP and α-helical domains point in the same direction, and another was a *trans*-like conformation where they point in opposite directions. Cryo-EM structures of assembled AcrAB-TolC show AcrA to be in the *trans* conformation,[35,36] and locking AcrA in the *cis* conformation was proposed to compromise the assembly of the complex. Therefore, we analyzed both *cis*- and *trans*-populations of our simulations but found no statistical significance between either population, suggesting that neither Mg^{2+} or Na^+ binding bias, or enforce, either state (Table S3).

Several different biophysical techniques were used to investigate Mg^{2+} binding to AcrA and confirmed that Mg^{2+} is capable of binding AcrA in both neutral and acidic regimes: ITC demonstrated a ∼mM strength interaction at both neutral and mildly acidic regimes, CD revealed a Mg^{2+}-triggered secondary structure change within acidic conditions, which did not affect its global thermal stability, and native MS revealed that Mg^{2+} could likely form multivalent, non-covalent interactions to the protein,

Please cite this article in press as: Russell Lewis et al., Mg^{2+}-dependent mechanism of environmental versatility in a multidrug efflux pump, Structure (2024), https://doi.org/10.1016/j.str.2024.12.012

without causing aggregation or oligomerization. MD simulations were utilized to provide an atomistic view of Mg^{2+} binding sites, and in combination with the biophysical results and theoretical predictors such as AlphaFold3 and *Me*Bi*Pred*, help support that Mg^{2+} is a structural cofactor of AcrA. Intriguingly, considering that the *E. coli* periplasmic concentration of Mg^{2+} can be ~7 times higher than in the surrounding medium, when bacteria are within environments containing 0.03–10 mM $MgCl_2$, the periplasmic Mg^{2+} concentration will be in the range of 0.21–70 mM.[37] Mg^{2+} may therefore be recruited as a cofactor to AcrA to different degrees depending on the composition of the bacterial surroundings.

Mg^{2+} binding counteracts acid-triggered dynamics

To understand the suggested acid-selective influence of Mg^{2+} on AcrA structure further, we used bottom-up HDX-MS to define its backbone structural dynamics at pH 6.0 and pH 7.4, with and without $MgCl_2$. During bottom-up HDX-MS a protein sample is made accessible to D_2O solvent, with HDX initiated when backbone amide hydrogens are broken through structure fluctuations and/or unfolding. The sample is then quenched by a shift to acidic pH and a temperature drop, proteins are then digested into peptides via acid-functional protease treatment, and the degree of D-label incorporation measured by MS.[38] HDX is fast within unfolded and solvent-exposed regions and slow within protected and stably folded regions. Differential HDX-MS (ΔHDX) analysis was performed to localize D-label differences between two states at peptide-level structural resolution (Figure 2).[41] When comparing results collected at pH 6.0 to those at pH 7.4, all conditions were kept the same except the pH of the HDX buffers, all samples were quenched to the same final pH of 2.4, and labeling times were corrected according to Equation 2 (see STAR Methods and see table).[42]

In the absence of Mg^{2+}, acidification increased the backbone HDX throughout $AcrA^S$, most prominently observed progressively within the latest time incubations. The earliest time point shows less difference as well as localized stabilization within the αβ barrel domain, which is lost at the later time points. This supports that the overall protein fold is not significantly influenced, as global structure loss would result in considerable exposure of backbone amides to HDX at the earliest time point.[43] Instead, it suggests that an expanded temporal structural plasticity within more acidic conditions is occurring (Figure 2). Rare intersecting HDX uptake plots were found between pH 6.0 and 7.4 within the MP and α-helical domains (two peptides, 25–44 and 127–136, Figures 2A and 2D). This signifies a region where upon acidification some parts are partially protected initially, perhaps becoming more structured, and other parts become more dynamic.[44]

To further understand the effect of increased acidity on AcrA backbone dynamics in the absence of Mg^{2+}, differential root-mean-square fluctuations (ΔRMSF) between AcrA with His285 doubly protonated (resembling pH 6.0) and deprotonated (resembling pH 7.4) were measured from MD simulations (Figure 2C). Protonation of His285 led to an increase in RMSF across all four domains of AcrA; increased dynamics was most prominent in the αβ barrel and MP domains. The agreement of ΔRMSF, both extent and location, with the ΔHDX measurements supports that protonation of His285 alone dictates the structural mobility observed within more acidic conditions. Taken together, this suggests that, when considered in contexts where Mg^{2+} concentrations are limited, a more acidic periplasmic environment increases the global plasticity of AcrA.

Mg^{2+} has a key role in maintaining cell wall integrity of gram-negative bacteria especially.[45] Therefore, it is important to consider periplasmic protein structure-function relationships in the context of Mg^{2+}, especially when considering its varying abundance within different media. Moreover, in the human small intestine, increased luminal acidity enhances Mg^{2+} absorption.[19,46] We, therefore, investigated whether Mg^{2+} could influence the structural dynamics of AcrA within the two pH regimes (pH 7.4 and pH 6.0) previously tested.

ΔHDX experiments were first performed on $AcrA^S$ at pH 6.0 comparing HDX profiles ± $MgCl_2$ (Figure 3). Mg^{2+} had a significant stabilizing effect on $AcrA^S$, exhibited by decreased deuterium incorporation within areas across all four domains throughout the HDX time course. Most of the α-helical hairpin shows protection, whereas the other three domains have more limited portions of protection. Areas with insignificant ΔHDX suggest backbone dynamics within these regions are not affected by Mg^{2+}. Interestingly, there is protection on several flexible linkers between AcrA's domains; regions between the αβ barrel-MP domains (e.g., ^{45}VKTEPLQITTELPGRTSAY^{63}) and lipoyl-α-helical domains (e.g., ^{90}GVSLYQIDPATYQATY^{105}) displaying reduced HDX. These flexible linkers are known to be key for AcrA to freely position its four domains and change conformations.[35,47] It is likely, therefore, that any backbone restriction of these areas influences the functionally required tertiary structure conformer populations, which AcrA is capable of forming during efflux. MD analysis of protonated AcrA ± Mg^{2+} also revealed that AcrA backbone dynamics are significantly stabilized in the presence of Mg^{2+}, with reduced ΔRMSF across all four domains, which agrees with the ΔHDX (Figure 3C). Together this supports that within acidic conditions Mg^{2+} binding causes $AcrA^S$ to become more rigid across its backbone (Figure 3). This structural rigidification is perhaps a contributing factor to the small, but statistically significant, 16% reduction in length of $AcrA^S$ previously observed in the presence of $MgCl_2$ by dynamic light scattering (DLS) and velocity centrifugation.[23]

Surprisingly, Mg^{2+} had no significant effect on the HDX profile of AcrA at pH 7.4, suggesting that it does not stabilize the backbone dynamics in the same manner as observed under acidic conditions (Figure S6). MD simulations supported that Mg^{2+} did not stabilize $AcrA^s$ when His285 was deprotonated in the same manner as it did when His285 was protonated (Figure 3), with increased flexibility being observed in areas of the αβ barrel and MP domains instead (Figure S7). The structural effect of Mg^{2+}, therefore, appears to be pH-dependent, only significantly acting on the backbone dynamics of AcrA within acidic conditions, when His285 is protonated, to generate a structural plasticity more like that found in neutral conditions. Interestingly, within our MD simulations a higher number of Mg^{2+} ions, when compared to Na^+, reside near (within 7 Å) both protonated and deprotonated His285; this was the case even when His285 was mutated to an Ala residue (Table S3). The localization of Mg^{2+} to residues near His285 may be how Mg^{2+} enacts its influence over the local hydrogen bonding network managed by His285 (de)protonation.

Please cite this article in press as: Russell Lewis et al., Mg^{2+}-dependent mechanism of environmental versatility in a multidrug efflux pump, Structure (2024), https://doi.org/10.1016/j.str.2024.12.012

CellPress
OPEN ACCESS

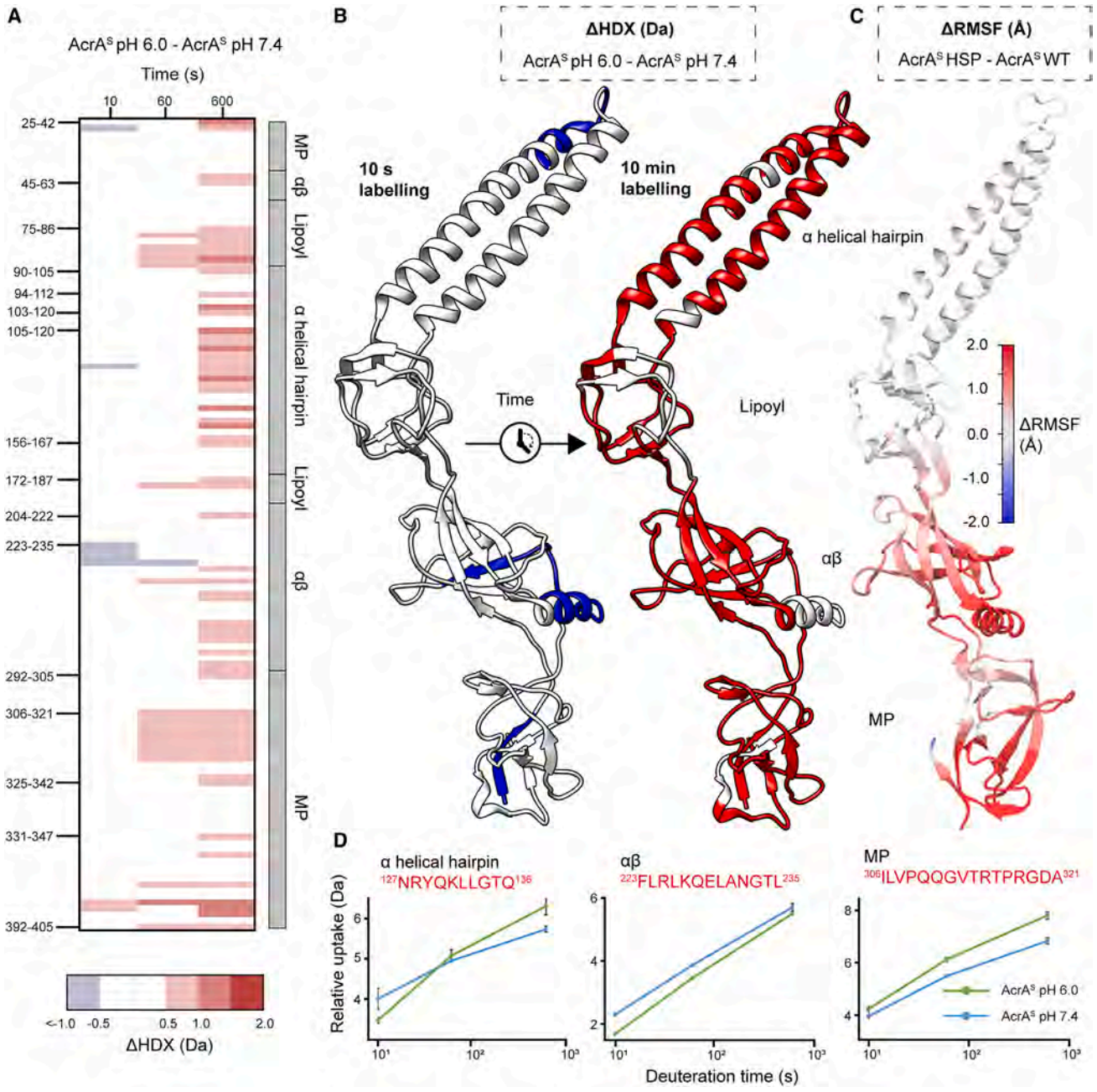

Figure 2. Structural dynamics of AcrA in the absence of $MgCl_2$ at pH 6.0 versus pH 7.4

(A) Chiclet plot displaying the differential HDX (ΔHDX) plots for AcrA^S pH 6.0 - AcrA^S pH 7.4. Blue signifies areas with decreased HDX between states, red signifies areas with increased HDX and white signifies areas with no significant change in HDX. Significance was defined to be $\geq$0.5 Da change with a p value $\leq$0.01 in a Welch's t test (n = 4). Boundaries of peptides within areas of significant changes are shown (left, y-axis) and AcrA features are labeled (right, y-axis).

(B) Regions with significant changes in ΔHDX are highlighted on the AcrA structure (increased and decreased HDX being red and blue, respectively) for the earliest and latest time points (PDB: 5O66) using HDeXplosion and Chimera.[39,40]

(C) AcrA colored according to the difference in root-mean-square fluctuations (RMSF) between simulations of the AcrA^S wild-type state and HSP (doubly protonated His285) state (AcrA^S HSP - AcrA^S WT), averaged over four replicas for each. Red indicates that the RMSF has increased whereas blue indicates it has decreased. RMSF was calculated over the last 70 ns of each 100-ns simulation.

(D) D-label uptake plots for three select peptides in different domains of AcrA. Uptake plots are the average deuterium uptake and error bars indicate the standard deviation (n = 4).

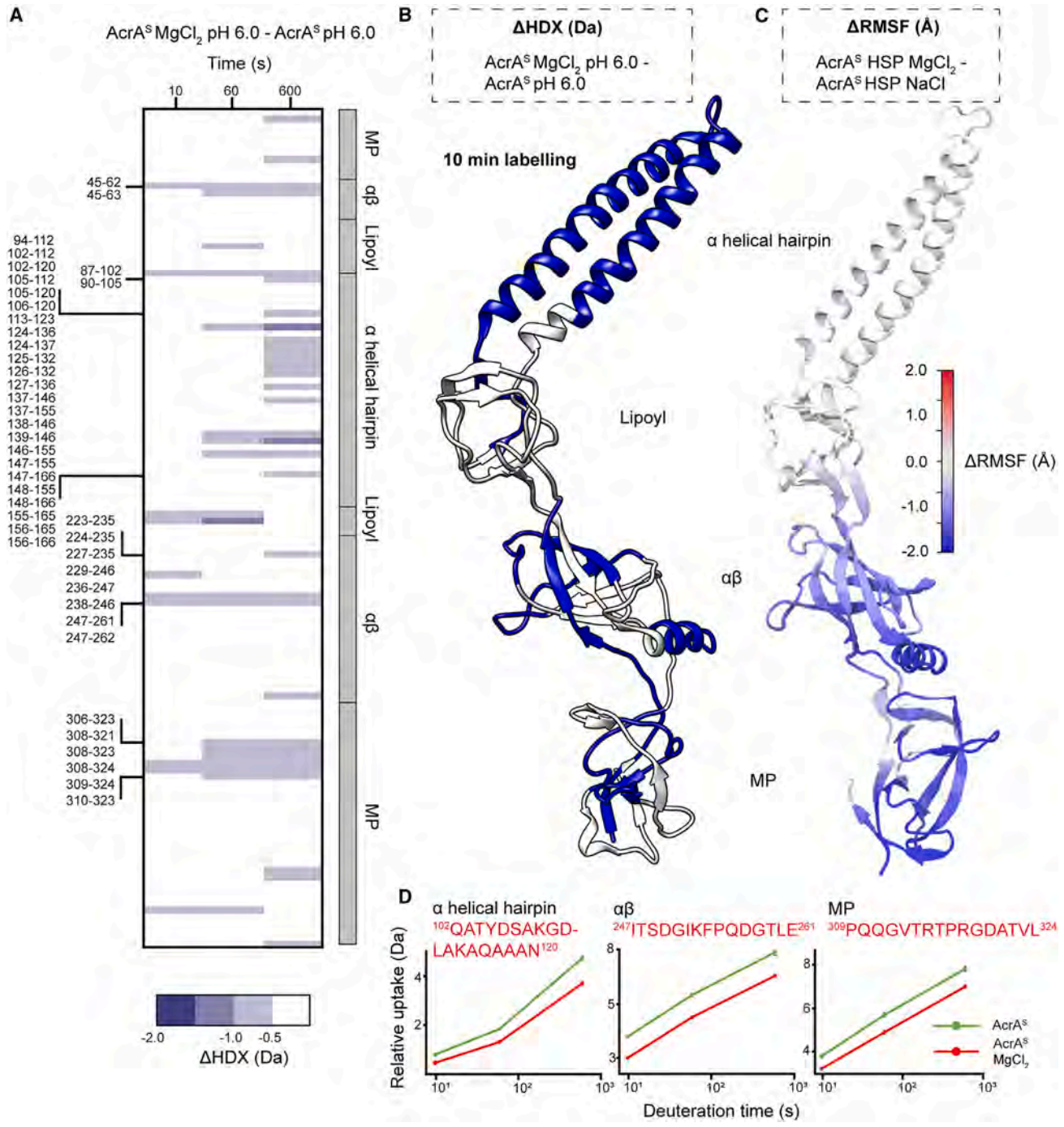

Figure 3. Influence of Mg^{2+} on the structural dynamics of AcrA at pH 6.0

(A) Chiclet plot displaying the differential HDX (ΔHDX) plots for (AcrA^S $MgCl_2$ pH 6.0) - (AcrA^S pH 6.0). Blue signifies areas with decreased HDX between states and white signifies areas with no significant change in HDX. Significance was defined to be $\geq$0.5 Da change with a p value $\leq$0.01 in a Welch's t test (n = 4). Boundaries of peptides within areas of significant changes are shown (left, y-axis) and AcrA features are labeled (right, y-axis).

(B) Regions with significant changes in ΔHDX are highlighted on the AcrA structure (increased and decreased HDX being red and blue, respectively) for the latest time point (PDB: 5O66) as performed in Figure 2B.

(C) AcrA colored according to the difference in RMSF between simulations of the AcrA^S HSP (doubly protonated His285) state in the presence of $MgCl_2$ and NaCl (AcrA^S HSP $MgCl_2$ - AcrA^S HSP NaCl), averaged over four replicas for each. Plots presented as in Figure 2C.

(D) D-label uptake plots for three select peptides in different domains of AcrA. Uptake plots are the average deuterium uptake and error bars indicate the standard deviation (n = 4).

Please cite this article in press as: Russell Lewis et al., Mg^{2+}-dependent mechanism of environmental versatility in a multidrug efflux pump, Structure (2024), https://doi.org/10.1016/j.str.2024.12.012

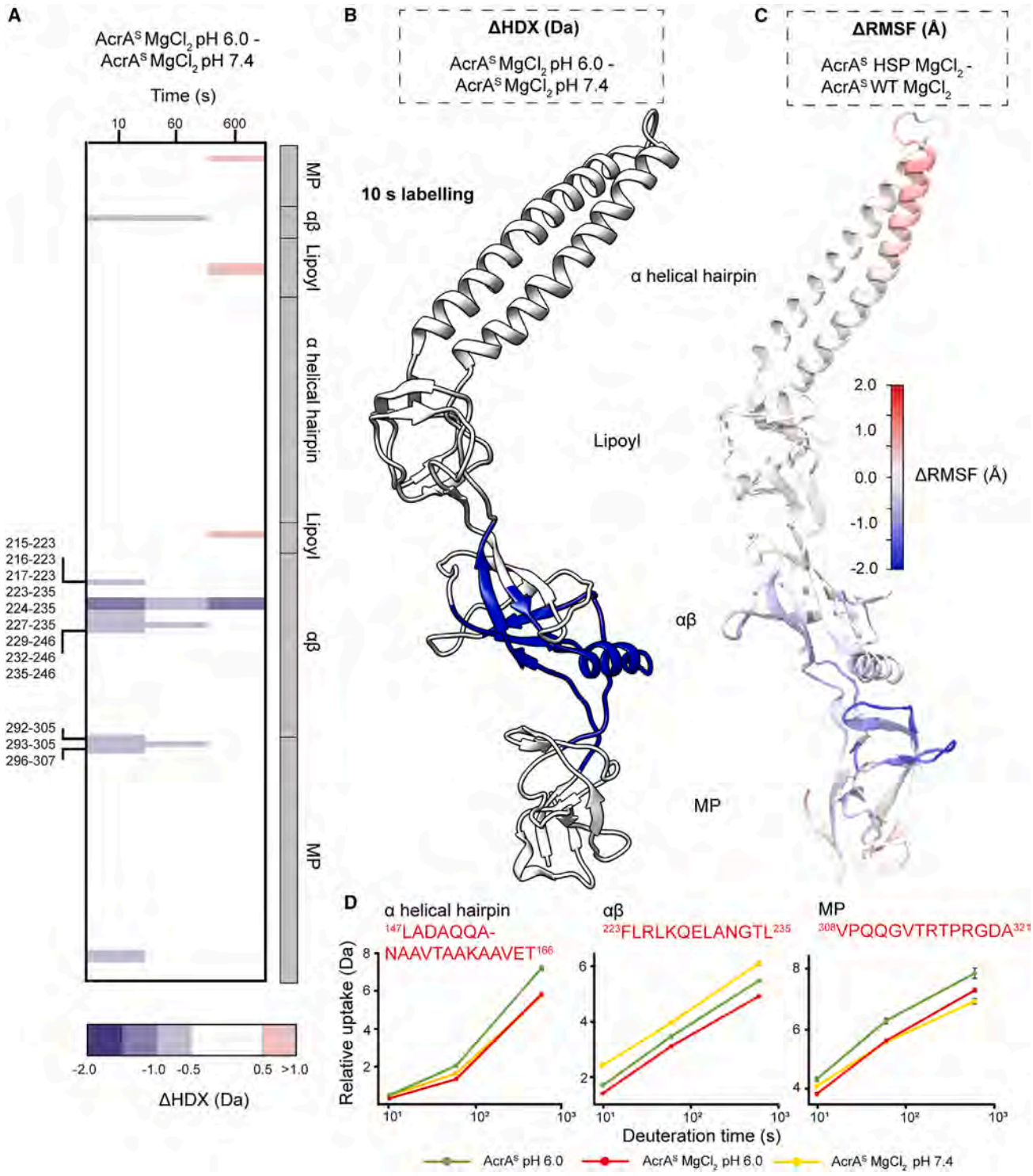

Figure 4. Effect of increased acidity on AcrA structural dynamics within a Mg^{2+} context

(A) Chiclet plot displaying the differential HDX (ΔHDX) plots for (AcrA^S $MgCl_2$ pH 6.0) - (AcrA^S $MgCl_2$ pH 7.4). Blue signifies areas with decreased HDX between states, red signifies areas with increased HDX between states and white signifies areas with no significant change in HDX. Significance was defined to be ≥0.5 Da change with a p value ≤0.01 in a Welch's t test (n = 4). Boundaries of peptides within areas of significant changes are shown (left, y-axis) and AcrA features are labeled (right, y-axis).

(B) Regions with significant changes in ΔHDX are highlighted on the AcrA structure (increased and decreased HDX being red and blue, respectively) for the earliest time point (PDB: 5O66) as performed in Figure 2B.

(legend continued on next page)

Please cite this article in press as: Russell Lewis et al., Mg^{2+}-dependent mechanism of environmental versatility in a multidrug efflux pump, Structure (2024), https://doi.org/10.1016/j.str.2024.12.012

His285 protonation leads to specific domain alterations within a Mg^{2+} context

To conclude the relationship between Mg^{2+} binding at neutral and mildly acidic conditions, ΔHDX was performed between the two pH states (pH 6.0 and pH 7.4) in the context of $MgCl_2$ (Figure 4). Greater HDX profile parity was observed between pH 6.0 and 7.4 conditions, further supporting that Mg^{2+} compensates for increased dynamics exhibited by $AcrA^S$ when His285 is protonated, with far fewer peptides possessing significantly increased HDX in the latest timepoint. However, from this ΔHDX analysis, more domain specific differences become pronounced, revealing pH-dependent stabilization within the αβ barrel domain (e.g., peptide ^{223}FLRLKQELANGTL^{235}), which is protected across the entire HDX time course. Interestingly, stabilization was prominent within the earliest HDX time point (10 s) (Figures 4A and 4B), which points toward His285 protonation leading to a backbone structural rearrangement, rather than conformational plasticity changes, which are typically observed at later time points like those observed for Mg^{2+} stabilization at pH 6.0 (e.g., 10 min, Figure 3). The CD data supports this (Figure S4F; Table S2), showing that secondary structure is significantly altered by a transition from pH 7.4 to 6.0, but only when $MgCl_2$ is present; without it then the global structural content remains similar. Within identical Mg^{2+} conditions MD simulations show reduced dynamics within similar sections of the αβ and MP domains when His285 is protonated, as well as increased dynamics of the α-helical hairpin tip (Figure 4C).

Importantly, these results partly decouple the effects of Mg^{2+} from pH effects on AcrA structural dynamics, revealing that increasing acidity leads to more specific alterations within both the αβ barrel and MP domains. These pH-induced structural changes may produce the conformational organization required for AcrA to function during efflux within more acidic contexts.

His285 is essential for maintaining pH-tolerant AcrA conformation and efflux pump activity

To analyze the effect of pH on AcrAB-TolC efflux activity *in vivo*, we constructed an AcrA His285Ala mutant ($AcrA^{H285A}$) and compared the activities of this mutant and the wild-type AcrA in efflux bacterial growth-dependent and -independent assays. In the antibiotic susceptibility assay, the efflux deficient *E. coli* Δ9 cells complemented with $AcrA^{H285A}$ variant were indistinguishable from cells complemented with the pump carrying the wild-type AcrA. Thus, at pH 7.4 the function of the pump is not compromised by His285Ala substitution (Table S4). The immunoblotting analysis of the complemented cells showed that the expression levels of $AcrA^{H285A}$ and the parent protein were similar (Figure S8).

Measurements of minimal inhibitory concentrations (MICs) at different pH are complicated by strong physiological responses as well as by physico-chemical properties of compounds and transmembrane diffusion. Hence, to analyze the effect of pH on efflux activity of AcrAB-TolC, we carried out the fluorescence probe efflux assay. In this assay, hyperporinated *E. coli* Δ9(Pore) cells carrying an empty vector or producing plasmid-borne AcrAB-TolC variants are incubated with increasing concentrations of probes, the fluorescence of which is enhanced when they bind to intracellular targets. As a result, the efflux activity is seen as lower fluorescence levels of the probes in efflux-proficient cells. As a probe, we used *N*-phenyl-naphthylamide (NPN), a non-ionizable membrane probe, which fluoresces when bound to the inner membrane of gram-negative bacteria. At four different pH values, 5.0, 6.0, 7.0 and 8.0, NPN rapidly accumulated in efflux-deficient cells as seen from similar kinetics of changes of fluorescence intensity (Figure S9) and the calculated steady-state accumulation levels (Figure 5A). Surprisingly, the wild-type AcrAB-TolC maintained NPN efflux at all four pH values (Figures 5B and S9). However, the efflux was the most efficient at pH 6.0–7.0 and declined by ∼50% at pH 5.0 and pH 8.0. Since the pKa of the imidazole ring of His285 is typically at ∼6, this result suggests that the optimal activity is when His285 exists in both the protonated and deprotonated states. In contrast, the activity of the pump assembled with $AcrA^{H285A}$ was strongly pH-dependent (Figures 5C and S9). Judging from the steady-state levels of NPN accumulation at the highest probe concentration of 32 μM, $AcrA^{H285A}$ was twice as efficient as the wild type at pH 7.0 and somewhat less at pH 8.0. However, $AcrA^{H285A}$ containing pump was ∼50% less efficient than the wild type at pH 6.0 and lost all its efflux activity at pH 5.0. Thus, the positively charged His285 in AcrA is required for the activity of AcrAB-TolC at acidic pH, whereas the alanine substitution in this position reduced the pH-dependence in this interface and was favourable at pH 7.0–8.0.

We also carried out the experiments in the presence and absence of $MgCl_2$. However, in agreement with previous studies we found that Mg^{2+} is needed for the stabilization of the outer and inner membrane lipid bilayers and the cells were leaky and unstable in the buffer pH 6.0 without $MgCl_2$ (Figure S10). As a result, no difference was seen between efflux-deficient and -proficient cells in the accumulation of NPN at pH 6.0. In the buffer pH 8.0 without $MgCl_2$, the pump assembled with the wild-type AcrA was not able to overcome NPN influx, whereas the $AcrA^{H285A}$ pump remained highly efficient (Figure S10). This result further supports that Mg^{2+} is required for wild-type AcrA function and the conclusion that alanine is preferred in the residue position 285 at pH 7.0 and above.

To confirm the importance and function of His285 under acidic conditions, we expressed and purified $AcrA^{H285A}$ (Figure S11) and performed HDX-MS experiments between the mutant and wildtype protein, as done previously. Specifically, we performed differential HDX-MS at pH 6.0 in the presence of $MgCl_2$ (Figures 5D and 5E), due to the discovered importance of Mg^{2+} in maintaining the backbone H-bonding network of AcrA (Figures 3 and 4). Between these conditions, $AcrA^{H285A}$ exhibited increased HDX compared to wildtype AcrA throughout parts of all its domains, with some more focused areas of reduced HDX within the MP and αβ domains (Figures 5D and 5E). This suggests that

(C) AcrA colored according to the difference in RMSF between simulations of the $AcrA^S$ wild-type state and HSP (doubly protonated His285) state, in a $MgCl_2$ environment ($AcrA^S$ HSP $MgCl_2$ - $AcrA^S$ WT $MgCl_2$), averaged over four replicas for each, presented as found in Figure 2C.
(D) Uptake plots for three peptides in different domains of AcrA. Uptake plots are the average deuterium uptake and error bars indicate the standard deviation (n = 4).

Please cite this article in press as: Russell Lewis et al., Mg^{2+}-dependent mechanism of environmental versatility in a multidrug efflux pump, Structure (2024), https://doi.org/10.1016/j.str.2024.12.012

CellPress
OPEN ACCESS

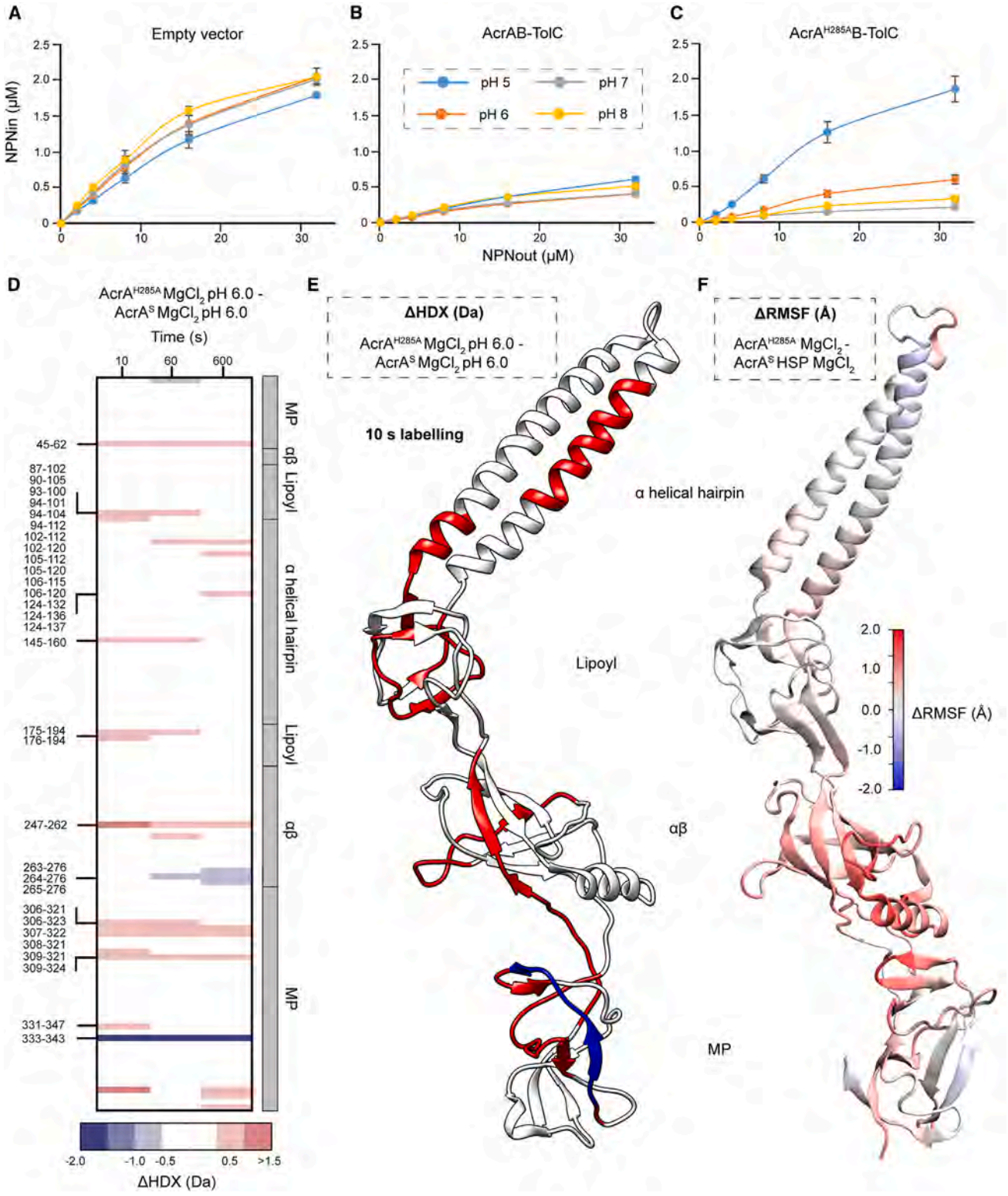

Figure 5. Investigating the function and dynamics of the AcrA^{H285A} mutant

Steady-state accumulation levels of the fluorescent probe NPN in *E. coli* Δ9(Pore) cells carrying an empty vector (A) or a vector containing wild-type (B) or AcrA^{H285A}B-TolC (C) as a function of the external NPN concentration. Cells were induced with 0.1% arabinose to express an outer membrane Pore, washed, and resuspended in buffer with indicated pH values and supplemented with 5 mM $MgCl_2$ and 0.1% glucose as an energy source. NPN was added in indicated

(legend continued on next page)

Please cite this article in press as: Russell Lewis et al., Mg^{2+}-dependent mechanism of environmental versatility in a multidrug efflux pump, Structure (2024), https://doi.org/10.1016/j.str.2024.12.012

the His285Ala mutation perturbs the structural dynamics of wild-type AcrA, even when Mg^{2+} is present, predominately making it more flexible in the MP domain (with several peptides between residues 306–324 showing increased HDX). Corresponding MD simulations supported the HDX findings (Figure 5F), with $AcrA^{H285A}$ exhibiting increased RMSF in all domains, particularly in the αβ barrel and MP domains as well as identifying the same small, stabilized sections of the MP and αβ barrel within $AcrA^{H285A}$.

Taken together, this offers a reasoning for the 50% reduced efflux efficiency by the His285Ala mutation at pH 6.0, through possible altered, allowable conformational sampling of AcrA during efflux. This could affect its ability to properly maintain critical contacts within the AcrAB-TolC complex and hinder the conformational transmission required for drug efflux. The combined *in vitro* and *in silico* structural data with the *in vivo* functional data validate the putative importance of the unique His285 residue as a pH-dependent conformational switch in AcrA. Its (de)protonation, in coordination with Mg^{2+} binding, appears to be essential for the pH-dependent (de)stabilization needed to ensure efficient efflux across different pH regimes.

The NSC 60339 inhibitor conformationally restricts AcrA in the presence of Mg^{2+}

Previously, we proposed a mechanism for the AcrA efflux pump inhibitor (EPI) NSC 60339.[14] Using a combination of HDX-MS, MD simulations and cellular efflux assays, we suggested that NSC 60339 acts as a molecular wedge between the lipoyl and αβ barrel domains of AcrA, reducing its structural dynamics across all four domains. Our previous work utilized HDX-MS investigations at pH 6.0, reflecting the often more acidic conditions of the periplasmic environment, where AcrA resides.[14] However, to investigate whether the inhibitor functions similarly with Mg^{2+} present, as it would be in the periplasm, HDX-MS experiments were repeated at pH 6.0, 1 mM $MgCl_2$, and ± 500 μM NSC 60339 (containing 5% DMSO to maintain drug solubility) (Figure S12). First attempts at collecting this dataset saw that the Mg^{2+}/DMSO combination induced extensive peptide carryover. Efforts to reduce carryover following previously described guidelines[38,48] were made and we obtained high-quality data from a pulsed HDX experiment using a 251s labeling reaction at pH 6.0 (83 peptides, 92.9% protein coverage). This analysis showed that similar key regions across multiple domains of $AcrA^{S}$ exhibited reduced structural dynamics by NSC 60339 in the presence of Mg^{2+}, for example ^{75}IILKRNFKEGSD^{86} in site IV and ^{308}VPQQGVTRTPRGDATVL^{32} in the MP domain away from site IV showed the characteristic strong HDX protection (Figure S12). Furthermore, regions that previously saw no change in HDX were also consistent. Therefore, it appears that NSC 60339 still inhibits AcrA via the same mechanism when Mg^{2+} is present, with inhibitor binding between lipoyl and αβ barrel domains enacting conformational restriction of AcrA throughout specific areas across its domains.

DISCUSSION

E. coli and other bacteria experience frequent changes in pH of their external media, whether it is a human host or waste waters. Since the periplasm is accessible for most ions, the outer membrane and periplasmic proteins are expected to be able to withstand the rapid changes in pH of the medium. Indeed, we found that AcrAB-TolC is functional in the pH range 5.0–8.0 with the optimum at pH 6.0–7.0. The conformational state of AcrA is critical for the activity of the pump and our findings show that binding of Mg^{2+} within AcrA and (de)protonation of His285 likely work together to modulate the conformational states and dynamics of AcrA within the AcrAB-TolC efflux pump (Figure 6).

Interestingly, His285 of AcrA is in the NSC 60339 efflux pump inhibitor binding site and is surrounded by aspartate and arginine residues, the hydrogen bonding to which is expected to be sensitive to the protonation state of His285. The imidazole ring of NSC 60339 has a positive charge on it and can interfere with bonding of the positively charged His285 or its rearrangement at acidic pH. Previous MD and docking showed that NSC 60339 H-bonds with the backbone of His285, not its imidazole ring.[49] Such binding to the backbone could prevent His285 from forming electrostatic interactions needed for the activity of AcrAB-TolC complex. The importance of these bonds is striking at pH 5.0, as the $AcrA^{H285A}$ variant, but not the wild type, is inactivated. HDX and MD simulations together support that His285 protonation alters the backbone dynamics of AcrA (in a Mg^{2+}-sensitive manner), suggesting that the positive charge on His285 leads to rearrangements of contacts.

All these data point to the critical role of the αβ barrel domain of AcrA, which is located between the AcrA funnel formed by the lipoyl and the α-helical hairpin on one side and the MP domain on the other. The funnel and the MP domain play distinct roles in AcrAB-TolC function, with the funnel acting on TolC to open it and the MP domain acting on AcrB and stimulating its functional rotations. The αβ barrel domain interfaces with the lipoyl and the MP domains are stabilized by H-bonding, which is particularly sensitive to changes in pH. The lipoyl domain does not interact with AcrB, whereas the αβ and MP domains form two different interfaces with the AcrB trimer. In the *trans* state

concentrations (NPNout) and fluorescence was measured in real-time for 10 min. Kinetic curves (Figure S8) were fitted into a two-exponential kinetic model to calculate the steady-state levels of intracellular NPN (NPNin). Plots are the mean and error bars indicate standard deviation (n = 3) from independent measurements.

(D) Chiclet plot displaying the differential HDX (ΔHDX) plots for ($AcrA^{H285A}$ $MgCl_2$ pH 6.0) - ($AcrA^{S}$ $MgCl_2$ pH 6.0). Blue signifies areas with decreased HDX between states, red signifies areas with increased HDX between states and white signifies areas with no significant change in HDX. Significance was defined to be ≥0.5 Da change with a p value ≤0.01 in a Welch's t test (n = 4). Boundaries of peptides within areas of significant changes are shown (left, y-axis) and AcrA features are labeled (right, y-axis).

(E) Regions with significant changes in ΔHDX are highlighted on the AcrA structure (increased and decreased HDX being red and blue, respectively) for the earliest time point (PDB: 5O66) as performed in Figure 2B.

(F) AcrA colored according to the difference in RMSF between simulations of the $AcrA^{H285A}$ and wild-type HSP (doubly protonated His285) state, in a $MgCl_2$ environment ($AcrA^{H285A}$ $MgCl_2$ - $AcrA^{S}$ HSP $MgCl_2$), averaged over four replicas for each, presented as found in Figure 2C.

Please cite this article in press as: Russell Lewis et al., Mg^{2+}-dependent mechanism of environmental versatility in a multidrug efflux pump, Structure (2024), https://doi.org/10.1016/j.str.2024.12.012

CellPress
OPEN ACCESS

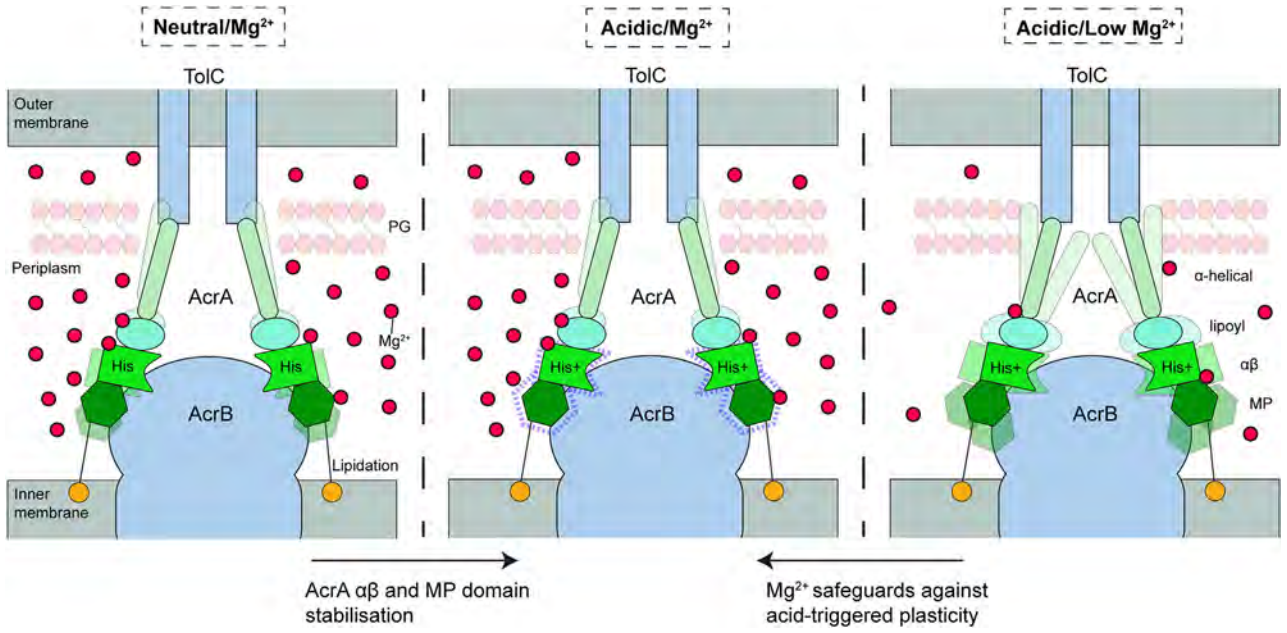

Figure 6. Proposed operational role of Mg^{2+} in modulating AcrA structural mobility to secure pump activity within acidic regimes

AcrA is a dynamic protein which ensures a sealed connecting pore between the AcrB transporter and the outer membrane factor TolC. Importantly, AcrA transmits conformational motions during substrate recognition and translocation by AcrB for the gating of TolC to enable drug export from the periplasm to the outside of the gram-negative bacterial wall. The periplasmic space has a pH like that of the external medium. When that external environment becomes more acidic, for example during enteric infection and colonization, then an acidified periplasmic space will occur and His285 becomes protonated. His285 is critical for modulating the hydrogen bonding network within AcrA. In a low Mg^{2+} environment AcrA undergoes a global increase in conformational plasticity which could prevent proper multidrug efflux pump function or pore concealment of its substrates. Whereas, within a Mg^{2+}-rich environment, at acidic pH, regions of the αβ barrel domain are stabilized and exhibit structural reorganization, likely to ensure proper function within increased acidity. PG, peptidoglycan layer.

of AcrA, seen in the cryo-EM structure of the resting AcrAB-TolC complex, the αβ barrel domain has only one contact with the MP domain.[35] The two domains have multiple contacts when the free AcrA is transitioning into the *cis* state.[34] The energy barrier between the two AcrA states is significant. In the *in situ* complex determined by cryo-ET, the interfaces of the αβ barrel domain of AcrA with the funnel and the MP domain have different states depending on the site of the interaction with AcrB.[12] The MP domain is slightly rotated (8°) and also moves up and down perpendicular to the membrane plane, the motion requiring the rearrangements of the contacts of the αβ barrel domain with the MP domain and the funnel. Our findings suggest that inactivation of AcrAB-TolC due to rigidification of AcrA's structure by NSC 60339 and the inactivation of $AcrA^{H285A}B$-TolC at pH 5.0 due to the loss of critical contacts might have the same underlying molecular mechanism: the loss of critical contacts of the αβ barrel domain needed for transmission of conformational changes between AcrB and TolC.

This work supports (de)protonation of the unique His285 residue coordinates the backbone H-bonding networks that dictate the conformational dynamics of AcrA. A His residue is found in a similar location in phylogenetically related PAPs, such as AcrA and its close homologs in Enterobacteriaceae, MexA and MexX (*Pseudomonas aeruginosa*), Adel (*Acinetobacter baumannii*), and others (Figure S13). However, more divergent members contain His residues in other domains (Table S5) that may or may not be contributing to pH-induced stabilization. Perhaps, this pH-triggered capability is tuned to specific environmental functions and niches the efflux pumps are overexpressed in and required for bacterial survival.[50–53] Significantly, we have shown that Mg^{2+} binding to AcrA broadly rectifies increased backbone dynamics exhibited under acidic conditions, facilitating pH-induced stabilization of the αβ barrel domain and its hinge region to the MP portion (Figure 6). As discussed above, the importance of this domain for pump function is well characterized; the localized stabilization of the αβ barrel domain, specifically in mildly acidic conditions, may offer a route to specialized conformations for robust efflux within these regimes. Mg^{2+} acting as a structural cofactor in this manner may be commonplace among other periplasmic adapter proteins, and thus multidrug efflux systems, to work across a variety of conditions the cell may exhibit.

RESOURCE AVAILABILITY

Lead contact

Further information and requests for resources and reagents should be directed to and will be fulfilled by the lead contact, Dr. Eamonn Reading (E.Reading@soton.ac.uk).

Materials availability

This study did not generate new unique reagents.

Data and code availability

- The HDX-MS data generated in this study have been provided as Data S1 and S2, and the HDX-MS summary tables have also been provided in Data S1. Furthermore, the mass spectrometry proteomics data have been deposited to the ProteomeXchange Consortium via the PRIDE partner repository with the dataset identifier PXD057200 and is publicly

available as of the date of publication. The accession code is also listed in the key resources table. The protein structures from other publications referenced in this paper are accessible under the PDB accession codes 5O66. The AlphaFold3 structure was generated from the UniProt entry P0AE06.

- This paper does not report original code.
- Any additional information required to reanalyze the data reported in this paper is available from the lead contact upon request.

ACKNOWLEDGMENTS

The studies at King's College London and the University of Southampton were supported by a UKRI Future Leaders Fellowship (MR/S015426/1 and MR/X009580/1) to E.R., a Wellcome Trust Investigator Award (214259/Z/18/Z) and a BBSRC Pioneer Award (BB/Y512849/1) to P.J.B., and a King's College London PhD studentship to B.R.L. The studies at University of Oklahoma and Georgia Institute of Technology were supported by the National Institutes of Health grant R01-AI052293 to H.I.Z. and J.C.G. Computational resources were provided through ACCESS (grant TG-MCB130173), which is supported by National Science Foundation (NSF) grants 2138259, 2138286, 2138307, 2137603, and 2138296. This work also used the Hive cluster, which is supported by the NSF (MRI-1828187) and is managed by the Partnership for an Advanced Computing Environment at Georgia Tech.

AUTHOR CONTRIBUTIONS

B.R.L., M.R.U, K.M.K, J.C.G., H.I.Z., and E.R. designed the project; B.R.L., L.M.N.S., D.H., and E.R. performed mass spectrometry experiments and analysis; B.R.L. and N.J.H. performed biophysical experiments and analysis; B.R.L., M.R.U., E.R., and H.I.Z. cloned, purified, and characterized all protein constructs; M.R.U. and H.I.Z. performed bacterial efflux and susceptibility assays and analysis; K.M.K. and J.C.G. carried out molecular dynamics experiments and post-molecular dynamics analyses; P.J.B., D.H., J.C.G., H.I.Z., and E.R. supervised and/or financially supported the project; B.R.L., M.R.U., K.M.K, J.C.G., H.I.Z., and E.R. wrote the manuscript with input from the other authors.

DECLARATION OF INTERESTS

The authors declare no competing interests.

STAR★METHODS

Detailed methods are provided in the online version of this paper and include the following:

- KEY RESOURCES TABLE
- EXPERIMENTAL MODEL AND STUDY PARTICIPANT DETAILS
- METHOD DETAILS
  - Cloning, expression, and purification
  - Circular dichroism
  - Hydrogen/deuterium exchange mass spectrometry
  - Native mass spectrometry
  - Metal-binding potential analysis
  - Site-directed mutagenesis and functional studies
  - Efflux assays
  - Molecular dynamics simulations
- QUANTIFICATION AND STATISTICAL ANALYSIS

SUPPLEMENTAL INFORMATION

Supplemental information can be found online at https://doi.org/10.1016/j.str.2024.12.012.

Received: June 20, 2024
Revised: November 15, 2024
Accepted: December 15, 2024
Published: January 13, 2025

REFERENCES

1. Global Leaders Group on AMR (2024). Towards specific commitments and action in the response to antimicrobial resistance. https://www.amrleaders.org/resources/m/item/glg-report.
2. Nikaido, H. (2009). Multidrug Resistance in Bacteria. Annu. Rev. Biochem. *78*, 119–146. https://doi.org/10.1590/S1807-59322011001000006.
3. Alav, I., Bavro, V.N., and Blair, J.M.A. (2021). Interchangeability of periplasmic adaptor proteins AcrA and AcrE in forming functional efflux pumps with AcrD in *Salmonella enterica* serovar Typhimurium. J. Antimicrob. Chemother. *76*, 2558–2564. https://doi.org/10.1093/jac/dkab237.
4. Tseng, T.T., Gratwick, K.S., Kollman, J., Park, D., Nies, D.H., Goffeau, A., and Saier, M.H. (1999). The RND permease superfamily: An ancient, ubiquitous and diverse family that includes human disease and development proteins. J. Mol. Microbiol. Biotechnol. *1*, 107–125.
5. Rice, L.B. (2008). Federal funding for the study of antimicrobial resistance in nosocomial pathogens: No ESKAPE. J. Infect. Dis. *197*, 1079–1081. https://doi.org/10.1086/533452.
6. Piddock, L.J.V. (2006). Multidrug-resistance efflux pumps — not just for resistance. Nat. Rev. Microbiol. *4*, 629–636. https://doi.org/10.1038/nrmicro1464.
7. Du, D., Wang-Kan, X., Neuberger, A., van Veen, H.W., Pos, K.M., Piddock, L.J.V., and Luisi, B.F. (2018). Multidrug efflux pumps: structure, function and regulation. Nat. Rev. Microbiol. *16*, 523–539. https://doi.org/10.1038/s41579-018-0048-6.
8. Wang, B., Weng, J., Fan, K., and Wang, W. (2012). Interdomain flexibility and pH-induced conformational changes of AcrA revealed by molecular dynamics simulations. J. Phys. Chem. B *116*, 3411–3420. https://doi.org/10.1021/jp212221v.
9. Ip, H., Stratton, K., Zgurskaya, H., and Liu, J. (2003). pH-induced Conformational Changes of AcrA, the Membrane Fusion Protein of *Escherichia coli* Multidrug Efflux System. J. Biol. Chem. *278*, 50474–50482. https://doi.org/10.1074/jbc.M305152200.
10. Fernando, D.M., and Kumar, A. (2013). Resistance-Nodulation-Division multidrug efflux pumps in Gram-negative bacteria: Role in virulence. Antibiotics *2*, 163–181. https://doi.org/10.3390/antibiotics2010163.
11. Zgurskaya, H.I., Weeks, J.W., Ntreh, A.T., Nickels, L.M., and Wolloscheck, D. (2015). Mechanism of coupling drug transport reactions located in two different membranes. Front. Microbiol. *6*, 100. https://doi.org/10.3389/fmicb.2015.00100.
12. Chen, M., Shi, X., Yu, Z., Fan, G., Serysheva, I.I., Baker, M.L., Luisi, B.F., Ludtke, S.J., and Wang, Z. (2022). *In situ* structure of the AcrAB-TolC efflux pump at subnanometer resolution. Structure *30*, 107–113.e3. https://doi.org/10.1016/j.str.2021.08.008.
13. Abdali, N., Parks, J.M., Haynes, K.M., Chaney, J.L., Green, A.T., Wolloscheck, D., Walker, J.K., Rybenkov, V.V., Baudry, J., Smith, J.C., and Zgurskaya, H.I. (2017). Reviving antibiotics: Efflux pump inhibitors that interact with AcrA, a membrane fusion protein of the AcrAB-TolC multidrug efflux pump. ACS Infect. Dis. *3*, 89–98. https://doi.org/10.1021/acsinfecdis.6b00167.
14. Russell Lewis, B., Uddin, M.R., Moniruzzaman, M., Kuo, K.M., Higgins, A.J., Shah, L.M.N., Sobott, F., Parks, J.M., Hammerschmid, D., Gumbart, J.C., et al. (2023). Conformational restriction shapes the inhibition of a multidrug efflux adaptor protein. Nat. Commun. *14*, 1–14. https://doi.org/10.1038/s41467-023-39615-x.
15. De Oliveira, D.M.P., Forde, B.M., Kidd, T.J., Harris, P.N.A., Schembri, M.A., Beatson, S.A., Paterson, D.L., and Walker, M.J. (2020). Antimicrobial resistance in ESKAPE pathogens. Clin. Microbiol. Rev. *33*, e00181-19. https://doi.org/10.1128/CMR.00181-19.
16. Miller, S.I., and Salama, N.R. (2018). The gram-negative bacterial periplasm: Size matters. PLoS Biol. *16*, e2004935. https://doi.org/10.1371/journal.pbio.2004935.

17. Nagy, T.A., Crooks, A.L., Quintana, J.L.J., and Detweiler, C.S. (2020). Clofazimine Reduces the Survival of *Salmonella enterica* in Macrophages and Mice. ACS Infect. Dis. *6*, 1238–1249. https://doi.org/10.1021/acsinfecdis.0c00023.

18. Wilks, J.C., and Slonczewski, J.L. (2007). pH of the cytoplasm and periplasm of *Escherichia coli*: Rapid measurement by green fluorescent protein fluorimetry. J. Bacteriol. *189*, 5601–5607. https://doi.org/10.1128/JB.00615-07.

19. Chamniansawat, S., Suksridechacin, N., and Thongon, N. (2023). Current opinion on the regulation of small intestinal magnesium absorption. World J. Gastroenterol. *29*, 332–342. https://doi.org/10.3748/wjg.v29.i2.332.

20. Alegun, O., Pandeya, A., Cui, J., Ojo, I., and Wei, Y. (2021). Donnan Potential across the Outer Membrane of Gram-Negative Bacteria and Its Effect on the Permeability of Antibiotics. Antibiotics *10*, 701. https://doi.org/10.3390/antibiotics10060701.

21. Groisman, E.A., Hollands, K., Kriner, M.A., Lee, E.-J., Park, S.-Y., and Pontes, M.H. (2013). Bacterial Mg^{2+} Homeostasis, Transport, and Virulence. Annu. Rev. Genet. *47*, 625–646. https://doi.org/10.1016/j.coph.2007.10.002.Taste.

22. Wang, T., Flint, S., and Palmer, J. (2019). Magnesium and calcium ions: roles in bacterial cell attachment and biofilm structure maturation. Biofouling *35*, 959–974. https://doi.org/10.1080/08927014.2019.1674811.

23. Zgurskaya, H.I., and Nikaido, H. (1999). AcrA is a Highly Asymmetric Protein Capable of Spanning the Periplasm. J. Mol. Biol. *285*, 409–420. https://doi.org/10.1006/jmbi.1998.2313.

24. De Angelis, F., Lee, J.K., O'Connell, J.D., Miercke, L.J.W., Verschueren, K.H., Srinivasan, V., Bauvois, C., Govaerts, C., Robbins, R.A., Ruysschaert, J.M., et al. (2010). Metal-induced conformational changes in ZneB suggest an active role of membrane fusion proteins in efflux resistance systems. Proc. Natl. Acad. Sci. USA *107*, 11038–11043. https://doi.org/10.1073/pnas.1003908107.

25. Bagai, I., Liu, W., Rensing, C., Blackburn, N.J., and McEvoy, M.M. (2007). Substrate-linked conformational change in the periplasmic component of a Cu(I)/Ag(I) efflux system. J. Biol. Chem. *282*, 35695–35702. https://doi.org/10.1074/jbc.M703937200.

26. Bas, D.C., Rogers, D.M., and Jensen, J.H. (2008). Very fast prediction and rationalization of pKa values for protein-ligand complexes. Proteins *73*, 765–783. https://doi.org/10.1002/prot.22102.

27. Tang, S., and Yang, J.J. (2013). Encyclopedia of Metalloproteins. In Encyclopedia of Metalloproteins (Springer Science), pp. 1243–1250.

28. Aptekmann, A.A., Buongiorno, J., Giovannelli, D., Glamoclija, M., Ferreiro, D.U., and Bromberg, Y. (2022). mebipred: identifying metal-binding potential in protein sequence. Bioinformatics *38*, 3532–3540. https://doi.org/10.1093/bioinformatics/btac358.

29. Sueki, A., Stein, F., Savitski, M.M., Selkrig, J., and Typas, A. (2020). Systematic Localization of *Escherichia coli* Membrane Proteins. mSystems *5*, e00808-19. https://doi.org/10.1128/msystems.00808-19.

30. Orfanoudaki, G., and Economou, A. (2014). Proteome-wide subcellular topologies of *E. coli* polypeptides database (STEPdb). Mol. Cell. Proteomics *13*, 3674–3687. https://doi.org/10.1074/mcp.O114.041137.

31. Abramson, J., Adler, J., Dunger, J., Evans, R., Green, T., Pritzel, A., Ronneberger, O., Willmore, L., Ballard, A.J., Bambrick, J., et al. (2024). Accurate structure prediction of biomolecular interactions with AlphaFold 3. Nature *630*, 493–500. https://doi.org/10.1038/s41586-024-07487-w.

32. Greenfield, N.J. (2006). Using circular dichroism spectra to estimate protein secondary structure. Nat. Protoc. *1*, 2876–2890. https://doi.org/10.1038/nprot.2006.202.

33. Micsonai, A., Wien, F., Bulyáki, É., Kun, J., Moussong, É., Lee, Y.H., Goto, Y., Réfrégiers, M., and Kardos, J. (2018). BeStSel: A web server for accurate protein secondary structure prediction and fold recognition from the circular dichroism spectra. Nucleic Acids Res. *46*, 315–322. https://doi.org/10.1093/nar/gky497.

34. Hazel, A.J., Abdali, N., Leus, I.V., Parks, J.M., Smith, J.C., Zgurskaya, H.I., and Gumbart, J.C. (2019). Conformational Dynamics of AcrA Govern Multidrug Efflux Pump Assembly. ACS Infect. Dis. *5*, 1926–1935. https://doi.org/10.1021/acsinfecdis.9b00273.

35. Du, D., Wang, Z., James, N.R., Voss, J.E., Klimont, E., Ohene-Agyei, T., Venter, H., Chiu, W., and Luisi, B.F. (2014). Structure of the AcrAB-TolC multidrug efflux pump. Nature *509*, 512–515. https://doi.org/10.1038/nature13205.

36. Kim, J.S., Jeong, H., Song, S., Kim, H.Y., Lee, K., Hyun, J., and Ha, N.C. (2015). Structure of the tripartite multidrug efflux pump AcrAB-TolC suggests an alternative assembly mode. Mol. Cell. *38*, 180–186. https://doi.org/10.14348/molcells.2015.2277.

37. Thanassi, D.G., Suh, G.S., and Nikaido, H. (1995). Role of outer membrane barrier in efflux-mediated tetracycline resistance of *Escherichia coli*. J. Bacteriol. *177*, 998–1007. https://doi.org/10.1128/jb.177.4.998-1007.1995.

38. Masson, G.R., Burke, J.E., Ahn, N.G., Anand, G.S., Borchers, C., Brier, S., Bou-assaf, G.M., Engen, J.R., Englander, S.W., Faber, J., et al. (2019). Recommendations for performing, interpreting and reporting hydrogen deuterium exchange mass spectrometry (HDX-MS) experiments. Nat. Methods *16*, 595–602. https://doi.org/10.1038/s41592-019-0459-y.

39. Zhang, N., Yu, X., Zhang, X., and D'Arcy, S. (2021). Structural bioinformatics HD-eXplosion: visualization of hydrogen – deuterium exchange data as chiclet and volcano plots with statistical filtering. Bioinformatics *37*, 1926–1927. https://doi.org/10.1093/bioinformatics/btaa892.

40. Pettersen, E.F., Goddard, T.D., Huang, C.C., Couch, G.S., Greenblatt, D.M., Meng, E.C., and Ferrin, T.E. (2004). UCSF Chimera — A Visualization System for Exploratory Research and Analysis. J. Comput. Chem. *25*, 1605–1612. https://doi.org/10.1002/jcc.20084.

41. Chalmers, M.J., Busby, S.A., Pascal, B.D., West, G.M., and Griffin, P.R. (2011). Differential hydrogen/deuterium exchange mass spectrometry analysis of protein-ligand interactions. Expert Rev. Proteomics *8*, 43–59. https://doi.org/10.1586/epr.10.109.

42. Li, J., Rodnin, M.V., Ladokhin, A.S., and Gross, M.L. (2014). Hydrogen−Deuterium Exchange and Mass Spectrometry Reveal the pH-Dependent Conformational Changes of Diphtheria Toxin T Domain. Biochemistry *53*, 6849–6856. https://doi.org/10.1021/bi500893y.

43. Fowler, M.L., McPhail, J.A., Jenkins, M.L., Masson, G.R., Rutaganira, F.U., Shokat, K.M., Williams, R.L., and Burke, J.E. (2016). Using hydrogen deuterium exchange mass spectrometry to engineer optimized constructs for crystallization of protein complexes: Case study of PI4KIIIβ with Rab11. Protein Sci. *25*, 826–839. https://doi.org/10.1002/pro.2879.

44. Morgan, C.R., and Engen, J.R. (2009). Investigating solution-phase protein structure and dynamics by hydrogen exchange mass spectrometry. Curr. Protoc. Protein Sci. *Chapter 17*, 17.6.1–17.6.17. https://doi.org/10.1002/0471140864.ps1706s58.

45. Silhavy, T.J., Kahne, D., and Walker, S. (2010). The Bacterial Cell Envelope. Cold Spring Harbor Perspect. Biol. *2*, a000414. https://doi.org/10.1101/cshperspect.a000414.

46. Heijnen, A.M., Brink, E.J., Lemmens, A.G., and Beynen, A.C. (1993). Ileal pH and apparent absorption of magnesium in rats fed on diets containing either lactose or lactulose. Br. J. Nutr. *70*, 747–756. https://doi.org/10.1079/bjn19930170.

47. Mikolosko, J., Bobyk, K., Zgurskaya, H.I., and Ghosh, P. (2006). Conformational flexibility in the multidrug efflux system protein AcrA. Structure *14*, 577–587. https://doi.org/10.1016/j.str.2005.11.015.

48. Ball, D., Nguyen, T., Zhang, N., and D'Arcy, S. (2022). Using hydrogen-deuterium exchange mass spectrometry to characterize Mtr4 interactions with RNA. Methods Enzymol. *673*, 475–516. https://doi.org/10.1016/bs.mie.2022.04.002.Using.

49. Darzynkiewicz, Z.M., Green, A.T., Abdali, N., Hazel, A., Fulton, R.L., Kimball, J., Gryczynski, Z., Gumbart, J.C., Parks, J.M., Smith, J.C., and Zgurskaya, H.I. (2019). Identification of Binding Sites for Efflux Pump Inhibitors of the AcrAB-TolC Component AcrA. Biophys. J. *116*, 648–658. https://doi.org/10.1016/j.bpj.2019.01.010.

50. McNeil, H.E., Alav, I., Torres, R.C., Rossiter, A.E., Laycock, E., Legood, S., Kaur, I., Davies, M., Wand, M., Webber, M.A., et al. (2019). Identification of binding residues between periplasmic adapter protein (PAP) and RND efflux pumps explains PAP-pump promiscuity and roles in antimicrobial resistance. PLoS Pathog. *15*, e1008101. https://doi.org/10.1371/JOURNAL.PPAT.1008101.

51. Lau, S.Y., and Zgurskaya, H.I. (2005). Cell division defects in *Escherichia coli* deficient in the multidrug efflux transporter AcrEF-TolC. J. Bacteriol. *187*, 7815–7825. https://doi.org/10.1128/JB.187.22.7815-7825.2005.

52. Schaffener, S.H., Lee, A.V., Pham, M.T.N., Kassaye, B.B., Li, H., Tallada, S., Lis, C., Lang, M., Liu, Y., Ahmed, N., et al. (2021). Extreme Acid Modulates Fitness Trade-Offs of Multidrug Efflux Pumps MdtEF-TolC and AcrAB-TolC in *Escherichia coli* K-12. Appl. Environ. Microbiol. *87*, 1–12. https://doi.org/10.1128/AEM.00724-21.

53. Zhang, Y., Xiao, M., Horiyama, T., Zhang, Y., Li, X., Nishino, K., and Yan, A. (2011). The Multidrug Efflux Pump MdtEF Protects against Nitrosative Damage during the Anaerobic Respiration in *Escherichia coli*. J. Biol. Chem. *286*, 26576–26584. https://doi.org/10.1074/jbc.M111.243261.

54. Krishnamoorthy, G., Wolloscheck, D., Weeks, J.W., Croft, C., Rybenkov, V.V., and Zgurskaya, H.I. (2016). Breaking the permeability barrier of *Escherichia coli* by controlled Hyperporination of the outer membrane. Antimicrob. Agents Chemother. *60*, 7372–7381. https://doi.org/10.1128/AAC.01882-16.

55. Phillips, J.C., Hardy, D.J., Maia, J.D.C., Stone, J.E., Ribeiro, J.V., Bernardi, R.C., Buch, R., Fiorin, G., Hénin, J., Jiang, W., et al. (2020). Scalable molecular dynamics on CPU and GPU architectures with NAMD. J. Chem. Phys. *153*, 044130. https://doi.org/10.1063/5.0014475.

56. Humphrey, W., Dalke, A., and Schulten, K. (1996). VMD: Visual Molecular Dynamics. J. Mol. Graph. *14*, 33-8–27-8. https://doi.org/10.1016/0263-7855(96)00018-5.

57. Tikhonova, E.B., Yamada, Y., and Zgurskaya, H.I. (2011). Sequential Mechanism of Assembly of Multidrug Efflux Pump AcrAB-TolC. Chem. Biol. *18*, 454–463. https://doi.org/10.1016/j.chembiol.2011.02.011.

58. Sørensen, L., and Salbo, R. (2018). Optimized Workflow for Selecting Peptides for HDX-MS Data Analyses. J. Am. Soc. Mass Spectrom. *29*, 2278–2281. https://doi.org/10.1007/s13361-018-2056-1.

59. UniProt Consortium (2023). UniProt: the Universal Protein Knowledgebase in 2023. Nucleic Acids Res. *51*, 523–531. https://doi.org/10.1093/nar/gkac1052.

60. Loos, M.S., Ramakrishnan, R., Vranken, W., Tsirigotaki, A., Tsare, E.P., Zorzini, V., Geyter, J.D., Yuan, B., Tsamardinos, I., Klappa, M., et al. (2019). Structural basis of the subcellular topology landscape of *Escherichia coli*. Front. Microbiol. *10*, 1670. https://doi.org/10.3389/fmicb.2019.01670.

61. Tikhonova, E.B., and Zgurskaya, H.I. (2004). AcrA, AcrB, and TolC of *Escherichia coli* form a stable intermembrane multidrug efflux complex. J. Biol. Chem. *279*, 32116–32124. https://doi.org/10.1074/jbc.M402230200.

62. Westfall, D.A., Krishnamoorthy, G., Wolloscheck, D., Sarkar, R., Zgurskaya, H.I., and Rybenkov, V.V. (2017). Bifurcation kinetics of drug uptake by Gram-negative bacteria. PLoS One *12*, e0184671. https://doi.org/10.1371/journal.pone.0184671.

63. Jorgensen, W.L., Chandrasekhar, J., Madura, J.D., Impey, R.W., and Klein, M.L. (1983). Comparison of simple potential functions for simulating liquid water. J. Chem. Phys. *79*, 926–935. https://doi.org/10.1063/1.445869.

64. Balusek, C., Hwang, H., Lau, C.H., Lundquist, K., Hazel, A., Pavlova, A., Lynch, D.L., Reggio, P.H., Wang, Y., and Gumbart, J.C. (2019). Accelerating Membrane Simulations with Hydrogen Mass Repartitioning. J. Chem. Theor. Comput. *15*, 4673–4686. https://doi.org/10.1021/acs.jctc.9b00160.

65. Darden, T., York, D., and Pedersen, L. (1993). Particle mesh Ewald: An N·log(N) method for Ewald sums in large systems. J. Chem. Phys. *98*, 10089–10092. https://doi.org/10.1063/1.464397.

66. Huang, J., Rauscher, S., Nawrocki, G., Ran, T., Feig, M., de Groot, B.L., Grubmüller, H., and MacKerell Jr, A.D. (2017). CHARMM36m: An Improved Force Field for Folded and Intrinsically Disordered Proteins. Nat. Methods *176*, 139–148. https://doi.org/10.1038/nmeth.4067.CHARMM36m.

67. Hageman, T.S., and Weis, D.D. (2019). Reliable Identification of Significant Differences in Differential Hydrogen Exchange-Mass Spectrometry Measurements Using a Hybrid Significance Testing Approach. Anal. Chem. *91*, 8008–8016. https://doi.org/10.1021/acs.analchem.9b01325.

Please cite this article in press as: Russell Lewis et al., Mg^{2+}-dependent mechanism of environmental versatility in a multidrug efflux pump, Structure (2024), https://doi.org/10.1016/j.str.2024.12.012

STAR★METHODS

KEY RESOURCES TABLE

REAGENT or RESOURCE	SOURCE	IDENTIFIER
Bacterial and virus strains		
Escherichia coli C43 (DE3) *ΔacrAB*	Gift from Prof. Dr. Klaas Martinus Pos laboratory	https://www.theposlab.de/group/klaas-pos/
Escherichia coli DH5α	New England Biolabs	C2987H
Escherichia coli Δ9-Pore strain (*ΔacrB ΔacrD ΔacrEF::spc ΔemrB ΔemrY ΔentS::cam ΔmacB ΔmdtC ΔmdtF att*Tn7::mini-Tn7T Tpr *araC* ParaBAD *fhuAΔC/Δ4L*)	Krishnamoorthy et al.[54]	N/A
Chemicals, peptides, and recombinant proteins		
NSC 60339	MedChemExpress	HY-119172
Deposited data		
HDX-MS data of $AcrA^S$	This study	ProteomeXchange Consortium (PXD057200)
Oligonucleotides		
Primer: $AcrA^S$ H285A Forward GAACCCGGATGCGACTCTGCTGCC (Integrated DNA Technologies)	This study	N/A
Primer: $AcrA^S$ H285A Reverse GGGAAGATAGCGCGTAG (Integrated DNA Technologies)	This study	N/A
Recombinant DNA		
pET28a WT $AcrA^S$	Zgurskaya et al.[23]	N/A
pET28a H285A $AcrA^S$	This study	N/A
Software and algorithms		
ProteinLynx Global Server (v. 3.0.2)	Waters	https://waters.com
DynamX (v. 3.0)	Waters	https://waters.com
SigmaPlot 14.5	Grafiti	https://grafiti.com/sigmaplot-detail/
Chimera USCF	Petterson et al.[40]	https://www.cgl.ucsf.edu/chimera/
HDeXplosion (v. 1.2)	Zhang et al.[39]	https://hd-explosion.utdallas.edu/
*Me*Bi*Pred*	Aptekmann et al.[28]	https://services.bromberglab.org/mebipred/home
NAMD (v. 2.14/v. 3)	Phillips et al.[55]	https://www.ks.uiuc.edu/Research/namd/2.14/ug/
VMD	Humphrey et al.[56]	https://www.ks.uiuc.edu/Research/vmd/

EXPERIMENTAL MODEL AND STUDY PARTICIPANT DETAILS

$AcrA^S$ wildtype and H285A mutant were expressed in *E. coli* C43(DE3)*ΔacrAB* cells. Functional studies were completed in *E. coli* Δ9-Pore strain (*ΔacrB ΔacrD ΔacrEF::spc ΔemrB ΔemrY ΔentS::cam ΔmacB ΔmdtC ΔmdtF att*Tn7::mini-Tn7T Tpr *araC* ParaBAD *fhuAΔC/Δ4L*).

METHOD DETAILS

Cloning, expression, and purification

$AcrA^S$. $AcrA^S$ lacking the signal peptide residues 1-24, and the site of lipidation Cys25, was cloned in a pET28a plasmid with a 6xHis and LE amino acid linker.[23,57] $AcrA^S$ is purified from the cytoplasmic fraction as previously reported.[14,23]

$AcrA^S$ His285Ala ($AcrA^{H285A}$). The His285Ala mutant was introduced to the wildtype $AcrA^S$ pET28a plasmid using the Q5 Site-Directed Mutagenesis Kit from New England Biolabs. Mutagenic primer can be found in the key resources table. $AcrA^{H285A}$ was purified using the same protocol as the wildtype protein.

Circular dichroism

The circular dichroism (CD) experiments performed in this work were completed on a Chirascan V2 instrument. For standard CD scans, $AcrA^S$ was buffer exchanged into protein buffer (50 mM $NaHPO_4$, 150 mM NaCl, +/- 1 mM $MgCl_2$, pH 6.0). Proteins were analysed at a concentration of 0.32 mg/mL. A coverslip was used with a pathlength of 0.005 cm. Scans were repeated three times between wavelengths 185-280 nm. BeStSeL online algorithm analysed the secondary structure.[33]

$AcrA^S$ was buffer exchanged into the same buffer as before but diluted to 0.0075 mg/mL. Thermal melts were performed at 15 temperatures from 30-95°C, with 5°C increments to first identify where the transition from a folded state to an unfolded state occurs. Then a more accurate scan ranging between 40-60°C with 1°C increments was completed to find the melting point (T_m). From this scan, values at 222 nm were taken for each temperature and thermodynamic parameters calculated from the following equations.

$$f_D = \frac{y - y_F}{y_D - y_F} \quad \text{(Equation 1)}$$

f_D is the fraction denatured, y_F is the gradient of folded protein and y_D is the gradient of the denatured protein. Spectra analysed on SigmaPlot.

Hydrogen/deuterium exchange mass spectrometry

Bottom-up HDX-MS experiments were performed on a nanoAcquity ultra-performance liquid chromatography (UPLC) Xevo G2-XS QTof mass spectrometer system (Waters). Optimised peptide identification and peptide coverage for $AcrA^S$ was performed from undeuterated controls. The optimal sample workflow for HDX-MS of $AcrA^S$ was as follows: 5 μl of $AcrA^S$ (20 μM) was diluted into 95 μl of either equilibration buffer (50 mM sodium phosphate, 150 mM NaCl, ± 1 mM $MgCl_2$, pH 6.0/pH 7.4) or labelling buffer (deuterated equilibration buffer) at 20°C. For accurate comparison between the two pH ranges, each labelling time at pH 7.4 was amended for pH 6.0 due to the slower rate of H/D exchange, using Equation 2 and shown in see below table.[42] Therefore, at pH 6.0, the labelling times were increased by a factor of 25.1. All figures display the pH 7.4 labelling times for clarity.

Hydrogen/Deuterium Exchange Reaction Time Table (in seconds)

HDX reaction condition labeling times	
pH 6.0 ($x10^{1.4}$)	pH 7.4 (standard)
251	10
1507	60
15071	600

Exchange (deuteration) times were corrected to the standard condition at pH 7.4 shown in the second column of the table. The number in the brackets in the first column is the time conversion factor for the corresponding pH condition. Temperature was maintained at 20°C.

$$\frac{K_{ch1}}{K_{ch2}} = \frac{[OH^-]_1}{[OH^-]_2} = \frac{K_w/[H^+]_1}{K_w/[H^+]_2} = \frac{10^{-pH_2}}{10^{-pH_1}} = 10^{pH_1 - pH_2} \quad \text{(Equation 2)}$$

After fixed times of deuterium labelling, the samples were mixed with 100 μl of quench buffer (formic acid, 1.6 M GuHCl, 0.1% (w/v) Fos-choline, pH 1.9) to provide a quenched sample at pH 2.4. 70 μl of quenched sample was then loaded onto a 50 μl sample loop before being injected onto an online Enzymate™ pepsin digestion column (Waters) in 0.23% (v/v) formic acid in water (200 μl/min flow rate) at 20°C. The peptic fragments were trapped onto an Acquity BEH C18 1.7 μM VANGUARD pre-column (Waters) for 3 min. The peptic fragments were then eluted using an 8-35% gradient of 0.23% (v/v) formic acid in acetonitrile (40 μl/min flow rate) into a chilled Acquity UPLC BEH C18 1.7 μM 1.0 x 100mm column (Waters). The trap and UPLC were both maintained at 0°C. The eluted peptides were ionized by electrospray into the Xevo G2-XS QTof mass spectrometer. MS^E data were acquired with a 20–30 V trap collision energy ramp for high-energy acquisition of product ions. Argon was used as the trap collision gas at a flow rate of 2 mL/min. Leucine enkephalin was used for lock mass accuracy correction and the mass spectrometer was calibrated with sodium iodide. The online Enzymate™ pepsin digestion column (Waters) was washed three times with pepsin wash (1.5 M Gu-HCl, 4% (v/v) MeOH, 0.8% (v/v) formic acid, 0.1% (w/v) Fos-choline).

All deuterium time points and controls were performed in triplicate/quadruplicate. Sequence identification was performed from MS^E data of digested undeuterated samples of $AcrA^S$ using ProteinLynx Global Server 2.5.1 (PLGS) software (Waters). The output peptides were then filtered using DynamX (v. 3.0) using these parameters: minimum intensity of 1481, minimum and maximum peptide sequence length of 5 and 20 respectively, minimum MS/MS products of 1, minimum products per amino acid of 0.11, and a maximum MH+ error threshold of 5 ppm.[58] All the spectra were visually examined and only those with a suitable signal to noise ratio were used for analysis. The amount of relative deuterium uptake for each peptide was determined using DynamX

(v. 3.0) and are only corrected for back exchange when specified. The relative fractional uptake (RFU) was calculated from the following equation, where Y is the deuterium uptake for peptide a at incubation time (*t*), and D is the percentage of deuterium in the final labelling solution:

$$RFU_a = \frac{Y_{a,t}}{MaxUptake_a \; X \; D} \qquad \text{(Equation 3)}$$

Native mass spectrometry

$AcrA^S$ was buffer exchanged into a volatile solution (100 mM ammonium acetate, pH 6.0) using a centrifugal exchange device (Micro Bio-Spin 6, Bio-Rad) according to manufacturer's instructions native MS experiments were performed on a Synapt G2-Si mass spectrometer (Waters). The following instrument parameters, optimised to avoid ion activation and protein unfolding: capillary voltage: 1.6-3.0 kV, sampling cone: 30 V, trap DC bias; 15 V, trap collision energy: 2 V, transfer collision energy: 2 V. Pressures were set to 5.91 $x10^{-2}$ mbar in the source region (backing) and to 1.58 x 10^{-2} in both trap and collision cells. The collision gas was Helium.

Metal-binding potential analysis

The *Me*Bi*Pred* (v 2.0) program[28] was used to identify metal-binding potential of protein sequences. All protein sequences analysed were abstracted from UniProt[59] and protein sequences which met the default cutoff of 0.5 within *mebipred* was considered an indication of metal-binding to either Fe, Ca, Na, K, Mg, Mn, Cu, K, Co, Ni metals (at this cutoff the first-tier model identified non-redundant metal-binding proteins with ~92% precision at 26% recall). Global localisation annotation for *Escherichia coli* K-12 proteins was acquired from Sueki et al.,[29] which utilize the database of the sub-cellular topology and localisation of the *Escherichia coli* polypeptides (https://stepdb.eu/)[30,60]; except MdtE which was redefined as an inner membrane lipoprotein (IMLP).

Site-directed mutagenesis and functional studies

The His285Ala amino acid substitution in AcrA was introduced by QuikChange II XL Site-Directed Mutagenesis Kit using p151AcrAB-His as the template.[61] Primer design and Polymerase chain reaction (PCR) reaction for each substitution were performed by following manufacturer's protocol.

E. coli Δ9-Pore strain (Δ*acrB* Δ*acrD* Δ*acrEF::spc* Δ*emrB* Δ*emrY* Δ*entS::cam* Δ*macB* Δ*mdtC* Δ*mdtF att*Tn7::mini-Tn7T Tpr *araC* ParaBAD *fhuA⊿C/⊿4L*)[54] was used in antibiotic susceptibility and efflux assays. For these assays, Δ9-Pore cells were transformed with an empty pUC18 vector, $p151AcrAB^{His}$ or its $p151AcrA^{H285A}B^{His}$ derivative. Susceptibilities to novobiocin, SDS, erythromycin and vancomycin were determined by two-fold broth microdilution as described before.[14]

Efflux assays

Overnight cultures of *E. coli* Δ9-Pore cells carrying pUC18, $p151AcrAB^{His}$ or $p151AcrA^{H285A}B^{His}$ plasmids were sub-cultured into a fresh LB medium supplemented with ampicillin (100 μg/ml final concentration) and incubated at 37°C with aeration until OD_{600} reached 0.1-0.3. The expression of the Pore was induced by addition 0.1% (w/v) L-arabinose and incubation for another 4 hours to reach OD_{600} ~1.0.

Cells were washed with HMG buffer (50 mM HEPES-KOH buffer pH 7.0, 1 mM magnesium sulfate and 0.4 mM glucose) and resuspended in HMG buffer pH 5.0, 6.0, 7.0 or 8.0 to an OD_{600} of ~1.0, at room temperature. Increasing concentrations of NPN were added to measure the substrate efflux efficiency of efflux-deficient Δ9-Pore(pUC18) and Δ9-Pore cells overproducing AcrAB or $AcrA^{H285A}B$ pumps. Kinetics of intracellular accumulation of NPN was monitored in at λex = 350 nm and λem = 405 nm in real time. Data was normalized and kinetic parameters were calculated as described previously using a MATLAB program.[62] Briefly, the time courses of NPN uptake (Figure S9) were fit to the burst-single exponential decay function $F = A_1 + A_2 \cdot (1-\exp(-kt))$, where A_1 and A_2 describe the magnitude of the fast and slow steps, respectively, and k is the rate of the slow step. The fast and slow steps were attributed to NPN binding to the cell surface and in the inner membrane, respectively.

Molecular dynamics simulations

To investigate the effects of pH and ion content on the AcrA monomer, twelve distinct systems were built and simulated using MD (Table S6). The AcrA monomer was initiated in either the cis or trans conformation.[34] The systems were built in TIP3P water boxes of uniform dimensions of 171 Å per side and ionized with either 0.15 M NaCl or 0.15 M $MgCl_2$.[63] The systems were ~470,000 atoms each. His285 was singly protonated to reflect the pH 7.0 experimental conditions. To reflect pH 6.0 conditions, His285 was doubly protonated. An additional set of systems were built for the His285Ala mutation. Two replicas of each system were run for a total of 24 simulations and a net simulation time of 12 μs.

Each system was equilibrated with an initial minimization followed by (1) relaxation of the water and ion molecules for 1 ns and (2) relaxation of the protein sidechains for 1 ns. An additional minimization step was applied (5000 steps) before beginning the production runs. The equilibration steps were performed with NAMD 2.14 with the productions performed with NAMD3.[55] Hydrogen mass repartitioning was applied to enable a timestep of 4 fs.[64] All simulations were done at constant temperature (310K) with Langevin dynamics and a damping coefficient of 1/ps, at constant pressure (1 atm) with the Langevin piston barostat, and with periodic boundary conditions. Short range non-bonded interactions were cut off at 12 Å with the force-based switching function starting at 10 Å.

Please cite this article in press as: Russell Lewis et al., Mg^{2+}-dependent mechanism of environmental versatility in a multidrug efflux pump, Structure (2024), https://doi.org/10.1016/j.str.2024.12.012

Long range interactions were calculated with particle-mesh Ewald method with a grid density of $1/Å^3$.[65] The CHARMM36m force-field was used for the protein.[66]

All analysis and visualization were done with VMD.[56] In addition, analysis shown represents the averages of four replicas – across both *cis* and *trans* conformations and two replicas for each condition. RMSF was calculated per residue over the last 470 ns of the simulation, discarding the first 30 ns as done previously.[14] In particular, trajectories with 10 frames per nanosecond were used to calculate the RMSF. The ΔRMSF values were calculated by first determining the average RMSF per condition, i.e. taking the average of the cis and trans conformations and of both replicas. Second, the average RMSF of one value was subtracted from the average RMSF of the other value. This provided a way to compare the dynamics observed in the MD simulations to the HDX experiments. The number of ions within 7 Å of each residue in the AcrA monomer was also calculated across the entire simulation. Root mean square deviation (RMSD) of each of the domains in AcrA was calculated for the backbone Cα atoms, and the rolling average over 25ns was plotted (Figures S14 and S15).

QUANTIFICATION AND STATISTICAL ANALYSIS

For HDX-MS analysis a significance level cut-off for experiments without biological replicates was set at 0.5 Da. This deuterium difference was greater than the confidence intervals calculated based on the pooled standard deviation values.[67] Only peptides which satisfied the corresponding ΔHDX cut-off and a P-value ≤ 0.01 in a Welch's t-test ($n = 4$) were considered significant. All ΔHDX structure figures were generated from the data using HDeXplosion and Chimera.[39,40] The HDX-MS data and the HDX-MS summary tables generated in this study have been provided as Data S1 and the HDX uptake plots as Data S2, as per consensus guidelines.